Full Waveform Inversion beneath the Central Andes: Insight into the dehydration of the Nazca slab and delamination of the back-arc lithosphere

Yajian Gao[1,2], Frederik Tilmann[1,2], Dirk-Philip van Herwaarden[3], Solvi Thrastarson[3], Andreas Fichtner[3], Benjamin Heit[1], Xiaohui Yuan[1], Bernd Schurr[1]

[1]GFZ German Research Centre for Geosciences, Potsdam, Germany
[2]Freie Universität Berlin, Berlin, Germany
[3]ETH, Zürich, Switzerland

Key Points:

- Normal dip subduction of the Nazca plate beneath the Central Andes
- Dehydration of the subducted Nazca plate, hydration of the mantle wedge and partial melting of the continental crust
- Underthrusting of the Brazilian Shield beneath the southern Altiplano and delamination beneath the southern Puna

Corresponding author: Frederik Tilmann, `tilmann@gfz-potsdam.de`

Corresponding author: Yajian Gao, `yjgao@gfz-potsdam.de`

Abstract

We present a new seismic tomography model for the crust and upper-mantle beneath the Central Andes based on multi-scale full seismic waveform inversion, proceeding from long periods (40–80 s) over several steps down to 12–60 s. The spatial resolution and trade-offs among inversion parameters are estimated through the multi-parameter point-spread functions. P and S wave velocity structures with a spatial resolution of 30–40 km for the upper mantle and 20 km for the crust could be resolved in the central study region.

In our study, the subducting Nazca slab is clearly imaged in the upper mantle, with dip-angle variations from the north to the south. Bands of low velocities in the crust and mantle wedge indicate intense crustal partial melting and hydration of the mantle wedge beneath the frontal volcanic arc, respectively and they are linked to the vigorous dehydration from the subducting Nazca plate and intermediate depth seismicity within the slab. These low velocity bands are interrupted at 19.8°–21°S, both in the crust and uppermost mantle, hinting at the lower extent of crustal partial melting and hydration of the mantle wedge.

The variation of lithospheic high velocity anomalies below the backarc from North to South allows insight into the evolutionary foundering stages of the Central Andean margin. A high velocity layer beneath the southern Altiplano suggests underthrusting of the leading edge of the Brazilian Shield. In contrast, a steeply westward dipping high velocity block and low velocity lithospheric uppermost mantle beneath the southern Puna plateau hints at the ongoing lithospheric delamination.

1 Introduction

The Andes is a long mountain belt across the entire western margin of the South American continent, extending for more than 6000 km (Figure 1). The subduction of the Nazca plate below South America along the Central Andes has resulted in drastic crustal shortening (Oncken et al., 2006) and thickening (X. Yuan et al., 2000; Heit, Sodoudi, et al., 2007; Heit et al., 2008), magmatism (Wörner et al., 1992; S. M. Kay et al., 1994; Wörner et al., 2000; S. M. Kay & Mpodozis, 2002; S. M. Kay & Coira, 2009) and lithospheric delamination (R. W. Kay & Kay, 1993; Whitman et al., 1996; Allmendinger et al., 1997; Beck & Zandt, 2002; Schurr et al., 2006; Bianchi et al., 2013; Beck et al., 2015; Scire, Biryol, et al., 2015; Garzione et al., 2017; J. Chen et al., 2020). The age of the subducting Nazca plate is ∼45–50 Ma at the trench (Müller et al., 2008) as it enters the subduction zone with a convergence rate of 61–65 mm/yr (Norabuena et al., 1999; Angermann et al., 1999). The subduction

of the Nazca plate initiated around 70-80 Ma and it is thought to have reached the lower mantle beneath the Central Andes ∼50 Ma ago, according to a recent plate reconstruction based on slab unfolding (Y. Chen et al., 2019).

The widest part of the Andean orogen is between 15° and 27°S, where the subduction angle is 20° - 30°, flanked southwards and northwards by the flat subduction segments, where the subducted Nazca plate flattens out to become nearly horizontal. The Altiplano and Puna plateaus together constitute the second largest high plateau in the world, the Central Andean Plateau (Figure 1), which is also the only one that formed under a subduction regime. The Altiplano plateau (AP), in the northern part of the Central Andean Plateau, is characterised by a single internally drained basin with an average rather uniform elevation around 3800 m, whereas the southern part of the Central Andean Plateau is the Puna plateau (PN), which exhibits a higher altitude around 4500 m with more rugged relief, enclosing a series of internal drained basins. The Central Andean Plateau is flanked to the west by the Western Cordillera (WC) and to the east by the Eastern Cordillera (EC), followed by the Subandean Ranges (SA), Santa Barbara System (SB) and the Sierras Pampeanas (SP) from the north to the south (Figure 1).

The formation of the Central Andean Plateau is thought to be linked to lithospheric foundering beneath the Central Andes (e.g., R. W. Kay & Kay, 1993; S. M. Kay et al., 1994; Beck & Zandt, 2002; McQuarrie et al., 2005; Garzione et al., 2006; DeCelles et al., 2015). Although many researchers agree on the existence of lithospheric foundering in the Central Andes, there remain vigorous debates on its mechanisms, scale, pattern, timing and surface expression. The tectonic history of the eastern margin of the Central Andes exhibits north-south variations, which might provide an insight into the lithospheric processes. North of 24°S, deformation in the EC is occurred between ∼40 and 15 Ma (McQuarrie et al., 2005; Oncken et al., 2006) before migrating to the SA after 10 Ma, forming a thin-skinned fold and thrust belt (Allmendinger & Gubbels, 1996; Allmendinger et al., 1997; Sobolev & Babeyko, 2005; Garzione et al., 2017; Ibarra et al., 2019). In contrast, south of 24°S, the back-arc deformation becomes thick-skinned in the SB and finally changes to the basement-cored uplift in the SP (Allmendinger & Gubbels, 1996; Allmendinger et al., 1997; Sobolev & Babeyko, 2005; Oncken et al., 2006; Garzione et al., 2017). The relations between Nazca plate subduction, foundering of the continental lithosphere and the latitudinal variations of deformation style within the back-arc are still poorly understood; further progress depends on a good understanding of the lithospheric structure.

The seismic structure of the crust and upper mantle beneath the Central Andes has been investigated by many tomographic studies, including regional body wave tomography (e.g., Schurr & Rietbrock, 2004; Schurr et al., 2006; Koulakov et al., 2006; Comte et al., 2016; Huang et al., 2019), teleseismic tomography (Heit et al., 2008; Bianchi et al., 2013; Scire, Biryol, et al., 2015; Scire, Zandt, et al., 2015; Scire et al., 2017) and surface wave and ambient noise tomography (Porter et al., 2012; Calixto et al., 2013; Ward et al., 2013, 2014; Delph et al., 2017; Antonijevic et al., 2016; Ward et al., 2016, 2017). Previous teleseismic and global tomography results revealed a continuous subducted Nazca slab from the uppermost mantle down to the lower mantle (Heit et al., 2008; Ritsema et al., 2011; Scire, Biryol, et al., 2015; Lei et al., 2020) with a potential slab tear at the southeastern edge of the Pampean flat subduction zone (Portner & Hayes, 2018). However, teleseismic tomography cannot easily separate anomalies in the crust and uppermost mantle due to smearing along steep ray-paths, such that the starting model and crustal corrections can exert a strong influence on the final results in this depth range. In contrast, local and regional earthquake tomography can provide more details for the crust and upper mantle in the selected regions but lacks resolution at larger depths. In some of these aforementioned regional tomographic studies, the upper part of the Nazca slab is visible as a relatively continuous high velocity anomaly beneath the Central Andes and various back-arc seismic structures were also imaged (e.g., Schurr et al., 2006; Bianchi et al., 2013; J. Chen et al., 2020). However, these studies were limited to small specific regions according to the footprints of the temporary seismic arrays, typically differing among each others in many methodological details, which makes margin-wide comparisons difficult. In order to obtain a large scale model for a wider part of the margin without losing details in the crust, we collect seismic waveform data from the previous temporary and permanent network stations deployed between 1988 and 2018 and integrate them into a multi-scale three-dimensional full waveform inversion (FWI) (e.g., Simutė et al., 2016; Krischer et al., 2018; Blom et al., 2020) to infer the seismic structure within the crust and upper mantle. Accurate simulations of seismic wave propagation through laterally heterogeneous models allows the calculation of accurate finite-frequency kernels with the adjoint method. (e.g., P. Chen et al., 2007; Fichtner et al., 2010; Tape et al., 2010; M. Chen et al., 2015; Simutė et al., 2016; Tao et al., 2018; Krischer et al., 2018; Blom et al., 2020; Xiao et al., 2020; Lei et al., 2020; van Herwaarden et al., 2021). Advances in the computational power make it feasible to invert the full waveform to image the seismic structure at regional scales down to relatively short periods, here 12 s.

In this study, we invert for the long-wavelength seismic velocity structures from the low frequency data first and progressively move to higher frequency waveforms, thereby avoiding strong dependence on the starting model. We present a new model of the seismic velocities in the crust and upper mantle beneath the Andean orogen between 14° and 30° S, from the coast until well into the backarc, in the southern part of the study region even reaching the Andean foreland, with depth resolution down to ∼250 km.

2 Data

We retrieved centroid hypocenters, origin times and moment tensors for over 600 events with magnitudes between M_W 5.0 and 7.0 within our study region from the Global Centroid-Moment-Tensor (GCMT) catalog (Ekström et al., 2012). Seismic waveforms were recorded by 26 permanent and temporary networks deployed at various periods between 1994 and 2018 (Figure 2b and Table 1). We packed the waveforms and meta data into one Adaptable Seismic Data Format (ASDF, Krischer et al., 2016) file for every event. Every complete ASDF container includes the seismic waveforms, the event information in QuakeML format (Schorlemmer et al., 2011) and the station information in StationXML format. As the computational cost for FWI scales with the number of the events, a practical approach is to maximize the amount of seismic waveform data for every event used in the study (Krischer et al., 2018). Thus, we exclude events with only few receivers or recorded only by short-period instruments. For each stage of the inversion, as it extends to shorter periods, we make a visual check of the remaining events, and remove some waveforms, which are noisy or which show obvious signs of cycle skipping compared to synthetics computed with the current model. Events that failed to provide enough reliable measurements after visual inspection were also deleted. Each event in the final dataset has been recorded by 20–100 stations. During pre-processing, the instrument responses were removed from the raw seismic data to obtain the ground displacement. Zero-phase third order Butterworth band pass filters with varying passbands were applied during the different stages of the inversion (see section 3).

3 Methods

Our waveform modeling and inversion is mainly based on the full waveform adjoint methodology (Tromp et al., 2005; Fichtner et al., 2009). Solutions of the visco-elastic wave equation in a radially anisotropic earth media are obtained from Salvus (Afanasiev et al., 2019), which is a suite of highly parallelised software performing full waveform modeling and inversion, which makes use of GPU acceleration and offers wavefield adapted meshes

Table 1. Seismic Network information

Code	Data Center	start	end	reference
C	IRISDMC	2007	2009	Chilean National Seismic Network
$C1$	IRISDMC	2012	-	Universidad De Chile (2013)
CX	GEOFON	2006	-	IPOC
GE	GEOFON	1993	-	GEOFON Data Centre (1993)
GT	IRISDMC	1993	-	Albuquerque Seismological Laboratory (ASL)/USGS (1993)
IQ	GEOFON	2009	-	Cesca et al. (2009)
IU	IRISDMC	1988	-	Albuquerque Seismological Laboratory (ASL)/USGS (1988)
WA	IRISDMC	2011	-	West Central Argentina Network
$2B$	GEOFON	2007	2009	Heit, Yuan, et al. (2007)
$3D$	GEOFON	2014	2016	Asch et al. (2014)
$5E$	GEOFON	2011	2013	Asch et al. (2011)
$8F$	GEOFON	2005	2012	Wigger et al. (2016)
$8G$	GEOFON	2013	2015	Salazar et al. (2013)
$X6$	IRISDMC	2007	2009	Sandvol and Brown (2007)
XE	IRISDMC	1994	1995	Silver et al. (1994)
XH	IRISDMC	1996	1997	Zandt (1996)
XP	IRISDMC	2010	2013	West and Christensen (2010)
XS	RESIF	2010	2013	Vilotte et al. (2011)
$Y9$	GEOFON	2007	2008	Sobiesiak and Schurr (2007)
YS	IRISDMC	2009	2013	Pritchard (2009)
ZA	GEOFON	2002	2004	Asch et al. (2002)
ZA	GEOFON	1994	1994	PISCO94
ZB	GEOFON	1997	1997	Schurr et al. (1997)
ZD	IRISDMC	2010	2013	Wagner et al. (2010)
ZG	IRISDMC	2010	2012	Beck et al. (2010)
ZL	IRISDMC	2007	2009	Beck and Zandt (2007)

(van Driel et al., 2020; Thrastarson et al., 2020). Compared to earlier works, we introduce some technical modifications of the inversion workflow and misfit functionals, with details presented below.

3.1 Parameterisation and starting model

The model is parameterized into velocities for vertically and horizontally propagating P waves (V_{PV} and V_{PH}) and vertically and horizontally polarised S waves (V_{SV},V_{SH}), density ρ and shear attenuation Q_μ (Figure 3). We extract an initial model from the second generation of the Collaborative Seismic Earth Model (CSEM, Fichtner et al., 2018). Specifically, the initial model consists of a global 1-D background model based on a modified Preliminary Reference Earth Model (PREM, Dziewonski & Anderson, 1981) including attenuation, where the 220-km discontinuity is replaced by a linear gradient. In the mantle, the 3-D S velocity perturbations from S20RTS (Ritsema et al., 1999) are superimposed on this model. Perturbations of the P velocity are scaled to S velocity using the relation proposed by Ritsema and van Heijst (2002). The crust is derived from the model of Meier et al. (2007). CSEM and thus our initial model also incorporate constraints from a previous large scale FWI work (Colli et al., 2013). Voigt averaged (Panning & Romanowicz, 2006) isotropic V_P and V_S of the initial model and their comparisons with the final model are illustrated within the supplementary material (S1-S2 and S4-S9).

Although the parameterisation specifies six parameters at each point not all can be resolved independently. In order to reduce the possible bias from a fixed density (Płonka et al., 2016; Blom et al., 2017), we update the density through the iterations but abstain from the interpretations due to the inferior resolution relative to the seismic velocity parameters. The number and type of velocity parameters being inverted for is varied through the stages of the multi-scale inversion (see section 3.3). Attenuation is fixed through the whole inversion. In this paper, we will focus on the interpretation of isotropic V_S, as this is the most robustly resolved parameter (see section 3.4). However, V_P is also fairly well resolved and is presented in the supplementary material without interpretation.

3.2 Misfit Functional

Various misfit functionals have been defined and applied in previous FWI studies (Q. Liu & Tromp, 2008; Kristeková et al., 2009; Fichtner, 2010; Tao et al., 2017; Y. O. Yuan et al., 2020). A reasonable and robust design for the misfit functional with its corresponding adjoint sources plays a crucial role in the convergence and final outcome of the inversion

(Fichtner, 2010). The main effect of the long-wavelength earth structure is to speed up or delay the arrival times of the seismic phases, but applying the classical L^2 misfit directly on the waveforms would introduce local minima, as the absolute amplitude recordings are less reliable than the phase measurements and the misfit is prone to be dominated by the outliers, thus placing strong demands on the quality of measurements. In addition, amplitudes are highly sensitive to the focal mechanism at some azimuths. At the other extreme, the cross-correlation time shift is probably the most widely used misfit measure in finite-frequency inversions. Its popularity results from the robustness of the measurement for the specific seismic phase shifts and its quasi-linear relation to the earth structure that facilitates the solution for tomographic inverse problems and overcomes the excessive non-linearity introduced by the L^2 (e.g., Luo & Schuster, 1991; M. Chen et al., 2015; Zhu et al., 2015; Y. Liu et al., 2017). However this method cannot fully exploit the distortion of the observed data due to the small scale heterogeneities or the interference of multiple phases (Fichtner, 2010; Tao et al., 2017). Although the L^2 waveform fit and cross-correlation time shift have been applied successfully in FWI, their applicability is limited to the cases where the seismic phases are clearly separable (cross-correlation time shift) or where the observed and the synthetic waveforms are very similar (L^2 waveform fit). Our work takes advantage of Time-Frequency Phase Shift misfits (Fichtner et al., 2008; Kristeková et al., 2009) for the first five inversion stages (Table 2). It is based on the transformation of both the observed and synthetic data into the time-frequency domain where the frequency-dependent phase shift misfits are measured and thus more waveform details are included than in the single cross-correlation time shift misfits. A significant advantage of this functional is the freedom of the time window selection, where it is no longer required to isolate particular seismic phases. The disadvantage of this approach is that additional care needs to be taken to avoid cycle skipping, especially for the higher frequency signals used in the final iteration stages. For the derivation of this misfit functional and corresponding adjoint sources, the reader is referred to Fichtner (2010).

In addition, we incorporate the Cross Correlation Coefficient (CCC) misfit into the high frequency stage of our inversion workflow (stage VI in Table 2), which provides another measurement of the discrepancy of the synthetic and observed data, where the relative amplitudes of different arrivals are taken into account and which is nevertheless little affected by the source or receiver properties (Tao et al., 2018). This method was introduced and used for 1-D waveform fitting by Matzel and Grand (2004) and then applied to FWI by Tao et al. (2017) and Tao et al. (2018).

The window selection is achieved with a semi-automatic algorithm, where the data are cross-correlated with the current synthetics within a sliding window and certain criteria are imposed on the cross correlation coefficients and time shifts for the window acceptance (Maggi et al., 2009; Krischer, Fichtner, et al., 2015). Following the automatic pre-selection, we visually checked and tuned the time-windows to avoid the cycle skipping aforementioned and fully exploit the distortion of the body wave phases due to small structure. The final acceptance criterion for every time window is the cross-correlation coefficient between the synthetic waveform and the observed ones should be larger than 0.6.

3.3 Multi-Scale inversion

The gradients of the misfit functional with respect to the model parameters are calculated using the adjoint method. The gradients can be used in various optimization schemes such as Conjugate-Gradients (CG) or L-BFGS (D. Liu & Nocedal, 1989), both of which we have implemented in our inversion work flow (see Appendix A and Table 2).

To obtain a global optimal solution and avoid the risk of being trapped in the local minimum, we follow a common approach of multi-scale inversion scheme (Bunks et al., 1995). Multi-scale FWI implies that we begin with the inversion from the long-period data for the long-wavelength seismic structure and march into the high-frequency domain to infer the small-scale structure. Through a multi-scale scheme, we could reduce the risk of the convergence to the local minima. We divide the whole inversion procedure into six stages (Table 2 and Figure 5c). For stages I–III, we use CG to update the model and observe clear drops of the misfits relative to the initial model whereas for stages IV–VI, we introduced the L-BFGS algorithm into the inversion in order to increase the convergence rate for the higher frequency inversion. We restart the CG or (and) L-BFGS for each stage, as the frequency contents, selected events and time windows and/or misfit functionals are adapted. The 20–80 s inversion was divided into two stages (III and IV) to accommodate additional time windows that are able to meet the selection criteria after the model was improved through stage III. For stages I–V, we use the time-frequency phase shift misfits (TF). Finally, in stage VI, we adopt the CCC misfit as the misfit function to measure the relative amplitudes, which capture effects from multi-pathing or scattering after most of the phase shifts have already been eliminated through the previous iterations. For the first five inversion stages (I–IV), isotropic V_P, V_{SV} and V_{SH} and density ρ are updated, whereas for the final two inversion stages (V and VI), we update V_{PV}, V_{PH}, V_{SV}, V_{SH} and density ρ simultaneously.

Table 2. Overview of inversion stages

No.	Periods	It.	Simulation time	Events	Windows	Optimization	Misfit
I	40–80 s	5	600 s	39	8130	CG	TF
II	30–80 s	7	600 s	53	9916	CG	TF
III	20–80 s	7	600 s	77	19211	CG	TF
IV	20–80 s	8	600 s	77	32753	L-BFGS	TF
V	15–80 s	10	600 s	117	37240	L-BFGS	TF
VI	12–60 s	7	600 s	117	37242	L-BFGS	CCC

We also build up a validation dataset to avoid the potential over-interpreting in the inversion dataset, which is independent of the inversion dataset thus not involved in the inversion procedure. The validation dataset consists in 30 events and provides 2164 unique ray-paths (Figure 5). Incorporation of the validation dataset could facilitate to identify the convergence due to an improved model should provide better fit to both the inversion and validation datasets (Lu et al., 2020). The evolution of the misfits within each stage is shown in Figure 5c. Surprisingly, during stage I and II the misfit reduction is actually slightly higher for the validation than the inversion subset. We believe this indicates that at the long periods (and thus wave lengths), there is essentially no overfitting and the exact misfit reduction is therefore controlled by the noise levels or the earthquake-station data coverage. The fact that the validation dataset improves more is thus coincidence; the important point is that the differences in fit between both sets are minor. In every stage, the evolution of the misfits for the validation dataset has a same trend as that of the inversion dataset, which illustrates the robustness of our multi-scale inversion scheme (Lu et al., 2020; Krischer et al., 2018).

Technically, in this work, we employ the Large-scale Seismic Inversion Framework 2.0 (LASIF, Krischer, Fichtner, et al. (2015), Thrastarson et al. (2021)) for the simulation management, which is a framework and toolkit for the adjoint FWI, especially designed for Salvus. In practice, we take advantage of this package to set up iterations, generate input files for the simulation submissions, select time windows and calculate misfits and adjoint sources between the observed and synthetic data. Model updates were carried out outside LASIF based on our own implementation of the CG and L-BFGS algorithms (Figure 4). Furthermore, in order to lower the effects of the uneven coverage of seismic stations, we

integrate the station weightings into the inversion, as implemented in LASIF (Krischer, Fichtner, et al., 2015; Thrastarson et al., 2021). The station weighting scheme takes fully account of the distances between neighboring stations and the number of the neighboring stations for every station. Every station weight thus is inversely proportional to the average distance with the other stations.

3.4 Model Assessment

In this subsection, we analyse the resolution for the inversion and the trade-offs among the parameter types. In traditional ray theory tomography, the checkerboard test is popular and relatively robust with low computational costs, but it is computationally prohibitive for FWIs. In this study, we therefore approximate the Hessian-vector product $\mathbf{H}\delta\mathbf{m}$ for a test function $\delta\mathbf{m}$ (Fichtner & Trampert, 2011; Fichtner & Leeuwen, 2015; Zhu et al., 2015, 2017; Tao et al., 2018)

$$\mathbf{H}\delta\mathbf{m} = \mathbf{g}(\mathbf{m} + \delta\mathbf{m}) - \mathbf{g}(\mathbf{m}) \tag{1}$$

where $\mathbf{g}(\mathbf{m})$ denotes the summed gradient from the adjoint simulations for model $\mathbf{m}$, whereas $\mathbf{g}(\mathbf{m}+\delta\mathbf{m})$ indicates the gradient from the perturbed model $\mathbf{m}+\delta\mathbf{m}$.

If the synthetics from the final model provide a good fit of the observed data and the inversion thus has reached convergence, $\mathbf{H}\delta\mathbf{m}$ can be used to estimate the model resolution. Specifically, when the $\delta\mathbf{m}$ is nearly point-localised, the $\mathbf{H}\delta\mathbf{m}$ will be a linearised point-spread function.

In order to provide a visual representation of resolution throughout the model rather than just for a single model node, we perturbed our model by adding velocity perturbations ($\delta\mathbf{m}$) in a three dimensional checkerboard pattern in the upper mantle made up of Gaussian spheres with $\pm 1\%$ maximum amplitude of the velocity for a specific depth and a Gaussian σ of 40 km. The horizontal and depth grid spacing of the Gaussian spheres are 2° and 100 km (Figure 6). We calculate $\mathbf{H}\delta\mathbf{m}$ for this anomaly pattern for V_{SV}, V_{SH} and isotropic V_P separately (Figure 6, 7, S10 and S11). For V_{SV} within the middle crust, we added similar Gaussian spheres but with σ=25 km at 20 km depth and a horizontal grid spacing of 1° in order to demonstrate the higher resolution at shallow depths.

Through the multi-parameter point-spread tests, we could confirm that the resolution in the crust is the highest (20 km). For the upper mantle, V_{SV}, V_{SH} and V_P could be resolved, although they suffer from weak smearing and some cross-talk between parameter classes, particularly between V_{SV} and V_{SH} (Figure 6). Therefore, we focus our interpretation on the

isotropic V_S model due to its better resolution but show the V_P model in the supplementary material (Figure S10). To further quantitatively assess the resolution, we also present the normalised product of the perturbations $\delta\mathbf{m}$ and the resultant Hessian product $\mathbf{H}\delta\mathbf{m}$ within and between parameter classes (Figure S12-S14).

3.5 Limitations

In this study, we do not invert for the earthquake sources but assume the centroid moment tensor solutions from the GCMT catalog to be correct. The reason is that our inversion domain is regional and many of our events are at the edge or outside the region covered by stations, implying a poor azimuthal coverage for the source inversion. Therefore the globally determined centroid solutions are likely to be better constrained than the regional moment tensor inversion. In order to mitigate the potential bias from mislocated events, we manually check and monitor the waveform fits, paying particular attention to the waveform polarities of the stations near the extension of the nodal planes of the earthquakes.

We further note that the wave propagation simulations are carried out on a regular spherical chunk mesh without taking into account the topography, ocean layer or explicitly meshed internal discontinuities. The periods covered in this study (12–60 s) mainly reflect the structure of the middle crust to the upper mantle and the effects of topography on the near surface structures could be negligible as the amplitude of the topography (4-6 km) for the Central Andean Plateau is much smaller than half of the minimum seismic wavelength (15 km) (Nuber et al., 2016). However, in the future work, we would add more constraints from topography and internal discontinuities into the higher frequency surface wave inversion. In addition, a more sophisticated weighting scheme could be introduced and compared to further balance and estimate the effects from the uneven data coverage (Ruan et al., 2019) to speed up the convergence.

4 Results

After 44 iterations, we obtain the final velocity model. The improved match between observed and synthetic waveforms for the final model are shown exemplarily for a few events and stations in Figure 8. Large and deep earthquakes in the slab below the foreland of the central Andes played a particular role in providing a diversity of ray path directions. Upgoing rays from these deep events do not only illuminate the slab and mantle wedge but due to their steep ray paths reduce the effect of lateral smearing in the crust and particularly upper mantle (Figure 8b).

Because of the upper limit (12 s) of the frequency bands and the inclusion of surface waves, the resolution of V_S is better than V_P, so we focus the presentation and discussion on the V_S model. Nevertheless, the V_P model is also valid and therefore the isotropic V_P model is presented in the supplementary material. Although both V_{SV} and V_{SH} were resolved separately and contain information on the radial anisotropic structure, we prefer to translate the V_{SV} and V_{SH} into isotropic V_S through the Voigt average (Panning & Romanowicz, 2006) to avoid bias from unevenly distributed ray paths. The model is displayed in Figures 9–14. Figures 9 and 10 show the horizontal sections at crustal and mantle depths, respectively. Absolute velocities are plotted for the crust but velocity perturbations relative to the isotropic 1D CSEM model (Figure 3) are used for the mantle to amplify the velocity variations. Figures 11–13 show detailed horizontal and vertical sections in the Peru flat subduction zone, the Central Andean normal dip subduction zone and the southern Puna, respectively; Figure 14 shows three along-strike cross sections. Locations for all cross-sections are shown in Figure 9b.

4.1 Seismic velocity structure of the crust

The striking feature in the crust (Figure 9) is a long band of low velocity anomalies extending from 16°S to 28°S, which closely follows the active volcanic arc. North of 23°S, this low velocity anomaly follows the boundary between the Altiplano (AP) and Western Cordillera (WC) and then extends southwest around the eastern boundary of the Atacama Basin (AB) into the southern tip of the WC. To facilitate the discussion, we divide this low velocity band into seven parts (low velocity anomaly C1-C7 in Figure 9a). C1 (from 16°S to 19.8°S) straddles the boundary of the AP and the WC, parallel to the coastline and the trench. South of 19.8°S, the amplitude of this low velocity anomaly decreases (marked as WAZ, Weak Amplitude Zone in Figure 9a), which coincides with a gap in the volcanic arc, the Pica Volcanic Gap (PVG), where no volcanic activity occurred since the Middle Pleistocene (Wörner et al., 1992, 2000). V_S within the WAZ ranges from 3.0 to 3.2 km/s, significantly higher than C1 and C2 where V_S=2.6–2.8 km/s (Figure 9, 12 and 14). South of the PVG (WAZ), the low velocity anomaly reappears as anomaly C2, coinciding with the reappearance of the active volcanoes. Anomaly C2 has previously been observed with regional body wave tomography (Koulakov et al., 2006; Schurr et al., 2006; Ward et al., 2013) and caused the appearance of a negative crustal converter in receiver function profiles across the Altiplano (X. Yuan et al., 2000; Wölbern et al., 2009). In the cross-section along 21°S (profile GG', Figure 12), we can observe strong lateral gradients or sub-vertical interfaces where the velocity drops in two steps from the forearc (FA) to the volcanic arc (70.5° W

to 68° W). The first sub-vertical interface separates the Central Depression (CD) from the forearc with the 4 km/s V_S contour, where the Mohorovičić (Moho) depth increases from 30 km to 50 km (X. Yuan et al., 2002; Wölbern et al., 2009; Tassara & Echaurren, 2012), whereas the second delimits the CD and the WC by the 3.6 km/s contour, accompanied by a further drop in the Moho from 50 km to 70 km. These interfaces are also characterized by a seismically active upper crust (Bloch et al., 2014; Sippl et al., 2018). The eastern interface also marks the position of the West Fissure (WF), a sub-vertical strike-slip faults system (Victor et al., 2004; Yoon et al., 2009), which connects with the eastern end of the Quebrada Blanca Bright Spot (QBBS), a thin and distinct strong west-dipping reflector at 20–30 km depth visible in the ANCORP reflection profile (Oncken et al., 2003; Yoon et al., 2009; Storch et al., 2016). In our model this reflector follows the -10 % perturbation contour in the crust beneath the CD (Figure 12e). Additionally, Yoon et al. (2009) and Storch et al. (2016) identified a nearly vertical reflector connecting the western edge of the QBBS with the upper interface of the Nazca slab, which was interpreted as the Fluid Ascent Path (FAP, Figure 12f). In our image, the FAP is surrounded by a 'nose' of low velocities in the mantle wedge, consistent with the earlier interpretation.

From 21.5°S to 23°S (Figure 9 and Profile HH' in Figure 12), the amplitude of the crustal low velocity anomaly attains its maximum value of the whole volcanic arc in both width and amplitude beneath the Altiplano-Puna Volcanic Complex (APVC) (anomaly C3). The APVC is a late Cenozoic large-volume silicic volcanic zone (de Silva, S. L., 1989) located at the transition between the AP and the higher and more rugged Puna plateau (PN). Parts of C3 have previously been observed in a joint inversion of surface waves and receiver functions (Ward et al., 2017), where also a very low V_S of 2.5 km/s was inferred. Beneath the AB (Figure 13), the crustal V_S is around 3.2–3.6 km/s, coinciding with the ambient noise tomography results (Ward et al., 2013). The frontal volcanic arc coincides with the western edge of C3. Both deviate from the overall trend of the arc and low velocity band, so that they appear to be shifted nearly 100 km landward at 23°S (Figure 9 and Profile II' in Figure 12). The area to the west is filled by the AB, which is characterised by fast crustal V_S of ∼3.2–3.6 km/s (Figure 13). South of 24°S, low velocity anomaly C4 (Figure 9 and profile JJ' in Figure 13) beneath the frontal volcanic arc is much weaker than its north counterparts (C1-C3) and strikes southwestward along the eastern boundary of the AB. Further south from 26°S to 27.5°S, the low velocity anomalies labelled with C5 and C6 display further decreased strength beneath the main volcanic arc. Beneath the southern PN along 25°S and 26°S (Profile KK'–LL' in Figure 13), we detect one isolated

low velocity anomaly (C7, V_S=2.8–3.2 km/s) beneath a back-arc volcanic center, the Cerro Galan Caldera (CGC) (S. M. Kay et al., 1994; S. M. Kay & Mpodozis, 2002; Delph et al., 2017).

Along the coast, a high velocity band marked as B is shown beneath the forearc from 19°S to 28°S, paralleling the trench and coastline (Figure 9) with V_S=3.6–4 km/s at 20–30 km depth (Figure 12). In the 40 km slice (Figure 9c), anomaly B presumably corresponds to the Nazca mantle lithosphere; as expected, its eastern edge approximately coincides with the top of the slab surface in Slab2.0, giving additional confidence in the resolving power of the inversion even slightly offshore. If we assume the V_S = 4.2 km/s contour as indicator of the Moho, we infer a forearc crustal thickness of 25-40 km, much thinner than the main arc beneath the WC, agreeing well with the Moho depth estimates from receiver functions (X. Yuan et al., 2002; Wölbern et al., 2009; Heit et al., 2014) and the density model with seismic constraints (Tassara & Echaurren, 2012).

4.2 Seismic velocity structure in the upper mantle

In the upper mantle, the most conspicuous feature is the strong positive velocity perturbation (anomaly H1 in Figure 10–13), which can be associated with the subducting Nazca plate. Its geometry varies from the southern edge of the flat subduction beneath South Peru (Figure 11c) to the normal dip subduction beneath Northern Chile (Figures 12 – 13) and then again the onset of the Pampean flat subduction at 28°S beneath Western Argentina (Profile NN' in Figure 13). These transitions are visible in a single along-strike cross-section, profile Q (Figure 14). In addition to the dominant slab anomaly H1, we detect several other anomalies in the mantle above the Nazca slab: beneath the back-arc region, we imaged high velocity anomalies located beneath the back-arc (H2 to H6) and low velocity anomalies from M1 to M9 (all visible in the map view in Figure 10 and back-arc profiles along R and S in Figure 14). In the following, we present these anomalies in detail and compare them with earlier studies.

4.2.1 Subducted Nazca plate and Mantle wedge

The transition from flat to normal-dip subduction of the Nazca slab occurs below South Peru and Bolivia (Figure 11). Due to limited ray coverage for South Peru, the resolution beneath this area is restricted to around 150 km depth (Figure 6). Beneath the Moho along Profile BB' (Figure 11), a large volume low velocity region extends from the off-shore into the back-arc beneath the AP. We separate this low velocity zone into three parts, M7 to

M9 (Figure 11); although they appear to be connected, they show noticeable differences in depth extent and spatial distribution. M7 extends from 50 to 100 km depth within the upper part of the Nazca plate, forming a necking feature in the slab (Ward et al., 2016) beneath the forearc. M9 beneath the frontal arc covers only a small depth range from 70 to 80 km and extends along the active volcanic arc in Southern Peru (Figure 11). In contrast, M8 spreads mainly beneath the back-arc, spanning the transition between the flat subduction and normal subduction regimes. M7 to M9 beneath South Peru share a high degree of similarity with the previous tomography results (Ma & Clayton, 2014; Ward et al., 2016; Antonijevic et al., 2015; Lim et al., 2018). South of M8, the uppermost mantle beneath the back-arc is instead dominated by a strong high velocity layer H4 at 80-120 km depth below the flat plateau of the northern AP (Ward et al., 2016). The transition from the flat to the normal-dip subduction is visible in Profile DD' (Figure 11) and appears to be accompanied by the increment of the velocities in the slab and decrease of the velocity within the crust beneath the volcanic arc (crustal low velocity anomaly C1 as illustrated in section 4.1).

For the seismic structure beneath Northern Chile from 19°S–23°S (Profile EE'- II', Figure 12), a continuous and normal-dip subducting Nazca slab is clearly imaged in our model (Anomaly H1). Although the first order features are almost the same for these five profiles, there are two differences we would like to highlight. In profile EE' and FF', the seismic velocity of the Nazca slab is less pronounced than in the other three profiles (GG'-II') and accompanied by a weaker lower plane of the double seismic zone (DSZ) (Sippl et al., 2018) and absence of intermediate depth seismicity cluster compared to profiles GG'-HH' (Figure 12 and 14a). The second difference is the variation of the strength of the low velocity anomalies within the mantle wedge. From the 80 km and 105 km slices and profile F-F'(Figures 10 and 12), there is a gap between low-velocity anomalies M1 and M2 from 19.8°S to 21°S under the PVG. The velocity range for the mantle wedge beneath the PVG is 4.4–4.6 km/s, while it is 4.2-4.3 km/s for M1 and M2. We remind that a similar gap in the low velocity anomalies appears in the middle crust (the WAZ) in this area, as discussed in section 4.1. South of 24°S, along profiles JJ'-NN' (Figure 13), the Nazca slab begins to flatten slightly southwards above 200 km. Large scale low velocity anomalies (M3–M5) are still present above the slab (Figure 10) but are replaced by higher velocities south of 27°S. Separate from these, a low velocity body M6 to the west of M3 (and north of ∼24°S) extends from 25 km down to 100 km depth, spanning from the lower crust of the overriding plate to the upper part of the Nazca slab, beneath the Coastal Depression (CD) and Domeyko Cordillera (DC) (Figure 13). The lower limit of M6 approximately follows the oceanic Moho

revealed by receiver functions (X. Yuan et al., 2000), which also indicated a slightly thicker-than-normal subducting oceanic crust. Therefore, the M6 appears to be confined to the oceanic crust and the fore-arc mantle wedge, possibly indicating a locally thicker and more hydrated oceanic crust (Ranero & Sallarès, 2004). Along profiles MM'-NN' (Figure 13), the Nazca plate reaches the northern edge of the Pampean flat subduction zone and the low velocity anomalies within the mantle wedge and middle crust are both much weaker than in the north. South of 28°S, there is a Holocene volcanic gap, where the frontal volcanic arc has been quiescent since 5 Ma (S. M. Kay & Mpodozis, 2002). Also, the amplitude of the high velocity Nazca slab decreases and the slab is less well confined compared to the North. However, this area is close to the boundary of our study domain, where the resolution is starting to diminish.

4.2.2 Continental lithosphere beneath the Altiplano (AP) and Puna (PN)

Discrete high speed anomalies are observed beneath the back-arc area including the AP and PN, which we mark as H2, H3, H5 and H6 (see Figure 10, Figure 12–14). Anomaly H2 beneath the eastern AP and EC extends from 19°S to 23°S (Figure 12) and is still visible at 130 km depth (Figure 10). It reaches a maximum thickness of 50 km at 22° S and thins rapidly south of 23°S, while it weakens gradually through its full depth extent to the north (Figure 14). H2 was also identified by regional tomography studies although only confined from 22.5°S to 24°S and interpreted as a delaminated block (Schurr et al., 2006; Koulakov et al., 2006). Teleseismic tomography with a linear array (Heit et al., 2008) along 21°S revealed a similar high speed anomaly under the depressed Moho beneath the AP and EC, validating the existence of high speed north of 22.5°S but without being able to constrain its along-strike extent. Using receiver functions and waveform modeling of deep eathquakes Beck and Zandt (2002) inferred a sub-Moho V_P of 8 km/s, which indicates lithosphere material.

An isolated cylindrical high velocity body H3 with velocity over 4.6 km/s is visible in the upper mantle down to ∼150 km below the northern edge of the Santa Barabara System (SB), connecting to a high velocity zone in the crust (Figures 10 and 13). Although this anomaly is situated close to the edge of the resolution domain and the resolution test indicates some smearing (Figure 6), H3 is better resolved than in previous works (Schurr et al., 2006; Ward et al., 2013; Scire, Biryol, et al., 2015). We tentatively attribute this high speed anomaly from the crust to the upper mantle as part of the Brazilian shield (Scire, Biryol, et al., 2015). More seismic observations are required for a precisely detailed

interpretation for this strong anomaly. Another high speed anomaly H5 beneath the EC thrusts westwards down to 150–200 km in depth beneath the southern PN (Figures 13 and 14) which has also been observed with teleseismic (Scire, Biryol, et al., 2015) and local tomography studies (Bianchi et al., 2013; Liang et al., 2014; J. Chen et al., 2020) but the inferred shapes differed between those studies. H5 is accompanied by westward thickening of the crust from the EC to PN (Tassara & Echaurren, 2012). Further south, high speed anomaly H6 locates beneath the northern Sierras Pampeanas (SP), occupying the entire lithosphere and merged with the flat Nazca slab along 27°S (Figure 10 and 13).

5 Discussion

5.1 Transition zone from the flat to the normal dip subduction beneath southern Peru

Although the study domain does not fully cover the flat subduction zone beneath Peru and Bolivia, the southeast tip of the flat subduction and the transition from the flat to the normal dip subduction zone are imaged clearly (Figure 11). The southeastern portion of the flat subducting Nazca slab is visible along profile AA' as a continuous high-velocity body down to the bottom of the resolved region (i.e., 150 km) but becomes low velocity and discontinuous in its upper part along BB' (M7) showing a necking feature. The slab necking was also reported by other tomography studies (Ma & Clayton, 2014; Ward et al., 2016) and with a high V_P/V_S ratio (Lim et al., 2018). The inland trace of the Nazca Fracture Zone seems delineating the northern boundary of M7, which is a narrow (25-50 km) oceanic fracture zone, marking the transition of the oceanic floor age from 45 Ma to 50 Ma. This fracture zone possibly introduces more fluids into the Nazca crust and mantle lithosphere than in the adjacent regions (Figure 11a). Thus, low-velocity anomaly M7 may represent oceanic crust that has not yet metamorphosed into eclogite facies and possibly includes part of the hydrated Nazca mantle lithosphere (Kim & Clayton, 2015; Ward et al., 2016). Additionally, two low velocity anomalies M9 and M8 (Figure 11a), beneath the frontal arc and back-arc, respectively, span a broad depth range from the continental Moho to the upper interface of the slab. M9 beneath the frontal arc extends down to over 80 km, deeper than could be resolved in previous surface wave tomography (Ward et al., 2016). M9 presumably represents a more strongly serpentinized mantle wedge (Ward et al., 2016); enhanced dehydration from the oceanic crust and lithosphere within the subducted Nazca fracture zone (M7) would be expected to introduce more fluids into the mantle wedge, causing not only serpentinization but also enhanced partial melting, thus explaining also

the low velocity anomalies in the continental crust (Figure 9). M8 beneath the backarc is a horizontal low velocity layer below the Moho, extending ∼100 km along strike, hinting at the absence of the continental lithophere of the upper plate. Ward et al. (2016) tentatively interpreted this anomaly as the concentration of fluids coming off the distorted slab. Based on our model, we do not preclude the possibility of the removal of the lithosphere due to the delamination, which would also explain the observed surface uplift since 9 Ma (Garzione et al., 2017).

Interestingly, in cross section CC' (Figure 11e), fast anomaly H4 has a similar depth extent (up to $\sim$ 100 km) as low velocity anomaly M8 in BB' (Figure 11g), when considering the velocity perturbations. We note the anti-correlation between the velocity within the uppermost mantle and topography, i.e., H4 is accompanied by the (relatively) lower topography in the AP and EC, while M8 is associated with the on average 4000 m high topography along BB', as qualitatively expected if the mantle lithosphere contributes to the isostatic balance (Ward et al., 2016). Two hypotheses were proposed to explain the presence of lithospheric material (anomaly H4) here. Either, it is the original mantle lithosphere of the AP (Ward et al., 2016), or it corresponds to the Brazilian Shield underthrusting from the East (Beck & Zandt, 2002; Ma & Clayton, 2015). Though coming up to the edge of the resolved region, H4 does seem to be connected with the lithosphere from the east beneath EC and Subandean Ranges (SA), so that our results favour the latter hypothesis.

5.2 Normal dip subduction zone and the dehydration of the Nazca Plate beneath the Northern Chile

We first review the key seismological observations related to the normal-dip subduction as we illustrated in the last section: (1) A weak low velocity zone within the uppermost mantle and middle crust (WAZ) from 19.8°S-21°S, coincides with the Pica Volcanic Gap (PVG): north and south to this gap, large amplitude low velocity anomalies emerge within the middle crust (anomalies C1 and C2) and the uppermost mantle (anomalies M1 and M2) beneath the active volcanoes (Figures 12 and 14); (2) The positive velocity anomalies within the slab at depth of 80-120 km are stronger and accompanied by a more vigorous DSZ and prominent intermediate depth seismicity cluster south of 21°S than further north (Figure 12) (Sippl et al. (2018)).

In receiver functions images a strong oceanic Moho converter has been observed (X. Yuan et al., 2000, 2002). Sippl et al. (2018) compared the locations of the upper plane of the DSZ with this converter and thus demonstrated that the upper plane DSZ seismicity locates

within the oceanic crust. Both DSZ and converter disappear down-dip at the same position and the DSZ is replaced with a dense intermediate-depth seismic cluster which was interpreted as indicating the completion of eclogitization of the oceanic crust (Sobolev & Babeyko, 1994; Bjørnerud et al., 2002; Hacker et al., 2003; Okazaki & Hirth, 2016; Sippl et al., 2018; Wagner et al., 2020). At 21°S (Figure 12), M2 locates above the intermediate-depth seismic cluster, so we interpret M2 as the hydrated mantle wedge. The dehydration of the oceanic lithosphere due to antigorite breakdown provides a plausible source of fluids. Here, the subducted mantle lithosphere probably contributes more fluids than the oceanic crust to the mantle wedge south of 21°S, causing vigorous partial melting in the continental crust and triggering the dense cluster of intermediate and deep seismicity within the oceanic lithosphere; even the deeper the slab is dried up and intermediate depth seismicity shuts off quickly downdip (Peacock, 2001; Ferrand et al., 2017; Sippl et al., 2018; Wagner et al., 2020).

A recent magnetotelluric study (Araya Vargas et al., 2019) inferred the crust and mantle wedge beneath the PVG to have higher electric resistivity, whereas from 21°S to 23°S, a large volume low resistivity body exists within the mantle wedge, extending from 50 km down to 100 km above the intermediate-depth seismicity cluster, confirming its hydrated state. Further supporting evidence comes from attenuation tomography, which revealed a high attenuation feature within the crust and uppermost mantle from 21°S to 23°S beneath the volcanic arc (Schurr et al., 2003). Combining the different extents of the partial melting within the crust, the hydration of the mantle wedge, the activity of the intermediate depth seismicity cluster and the electrical resistivity, we infer that the dehydration from the subducted Nazca lithosphere appears to be much more vigorous from 21-23°S than beneath the PVG.

The PVG extends from 19.8°S to 21°S, corresponding to a segment where the volcanic activity is absent since Middle Pleistocene (Wörner et al., 1992). Araya Vargas et al. (2019) proposed that the crust beneath the PVG represents a block with anomalously low permeability, which precludes circulation of magmas or fluids within the continental crust. Some authors have argued that the subducted Iquique Ridge (Figure 1), composed of several seamounts (Madella et al., 2018), is associated with enhanced hydration of the Nazca plate prior to entering the trench from 20°S–21°S (Comte et al., 2016; Sippl et al., 2018; Araya Vargas et al., 2019). However, in our model, higher velocities in the mantle wedge beneath the PVG indicate that it is drier than north and south of the gap. This observation suggests a much reduced slab dehydration (and wedge hydration) beneath the PVG. From

an anisotropic P wave tomography (Huang et al., 2019), the uppermost mantle at 60 km from 21° S to 23° S is characterised by trench-normal fast directions, while below the PVG trench-parallel fast directions are found, which presumably indicates the disruption of the flow pattern in the mantle wedge. The Iquique Ridge has been subducting since ∼2 Ma in this region (Rosenbaum et al., 2005) and its arrival is probably coeval with the formation of the PVG during the Holocene (Wörner et al., 1992). We therefore agree with previous studies that attribute the development of the PVG to the subduction of the Iquique ridge, but argue that this has diminshed hydration of the mantle wedge. There is therefore no need to invoke permeability variations in the lower crust to explain the absence of volcanism there. Interestingly, unlike the Nazca Ridge beneath south Peru and Juan Fernandez Ridge (Figure 1) beneath Pampean Chile, which are accompanied by prominent flat subductions of the Nazca plate, the subduction of the Iquique Ridge does not seem to influence the subduction angle or at least has not yet initiated a large scale flat subduction possibly due to the short subduction history of the Iquique Ridge. (Ramos & Folguera, 2009; Manea et al., 2017).

A wedge-like cluster of crustal seismicity (Sippl et al., 2018; Bloch et al., 2014) appears to overlap with the high velocity forearc crust and the shallow part of the Nazca slab (anomaly B, Figure 12c-j, profiles F-I). The eastern boundary of this seismicity cluster (equivalent to the 4 km/s V_S contour) is at or slightly east of the transition from the forearc to the CD. This fast crustal forearc is characterized by high electrical resistivity (Araya Vargas et al., 2019) and low attenuation (Schurr et al., 2006, 2003). The obervations thus indicate cold temperatures beneath the forearc and low interconnectivity of the interstitial fluids. The second lateral transition mentioned in section 4, the boundary between the CD and WC, is characterized by intense upper crustal seismicity (Figure 12c-h, profiles F-H). At the surface this location coincides with the West Fissure (WF) faulting and the western edge of the AP. Here, the electrical resisitivity is low all the way from the crust to the fore-arc mantle (Araya Vargas et al., 2019), where the low resistivity region connects to the slab at the onset of intermediate depth intra-slab seismicity. We further conclude that this sub-vertical transition might be related to upward migrating fluids from the mantle wedge to the overriding plate crust, where it modifies the rheological properties of the forearc crust from brittle in the west to ductile in the east (Bloch et al., 2014).

To summarize, from 18° S to 27° S, five low velocity anomalies M1 - M5 enclose the hydrated mantle wedge within the uppermost mantle beneath the frontal volcanic arc and cause the partial melting within the crust (C1-C5, Figure 14a).

5.3 Multi-stage continental lithospheric foundering and the evolution of the crustal magma chambers

High velocity anomaly H2, extending between 20.5°S and 23°S and down to 130 km in depth, represents a thin mantle lithosphere with a thickness of ∼50 km beneath the southern AP and northern PN. Receiver function images of the lithosphere-asthenosphere boundary (LAB) along 21°S (Heit, Sodoudi, et al., 2007) confirm this thickness estimate (black dashed line in Profile GG', Figure 12). We interpret this high velocity layer as the westward leading edge of the Brazilian shield that fills in the room left by the removal of the autochthonous lithosphere of the EC. Therefore, the Brazilian shield has reached beneath the EC and the east part of the southern AP (Beck & Zandt, 2002; McQuarrie et al., 2005; Scire, Biryol, et al., 2015). Meanwhile, the extent of the large scale Altiplano-Puna Magma Body (APMB, Ward et al., 2017, anomaly C3 in the crust from our nomenclature) beneath the APVC implies large scale partial melting, resulting in the largest magma reservoir on Earth (Ward et al., 2013, 2014, 2017). The thin lithosphere and additional fluid flux from enhanced hydration melting in the mantle wedge (see section 5.2) contribute to the flare-up of large volume ignimbrites and the overlying higher topographic dome (Perkins et al., 2016).

South of 24°S, the thinned lithosphere H2 finally disappears beneath the southern PN and is replaced by the low velocity uppermost mantle (Figure 13), possibly representing the upwelling asthenosphere and connected with the mantle wedge (M3-M5) beneath the frontal volcanic arc (Bianchi et al., 2013; Scire, Biryol, et al., 2015; Wang & Currie, 2015; J. Chen et al., 2020). However, in the deeper part of the upper mantle atop of the subducting Nazca plate, a high velocity anomaly H5 (Profile KK'–LL' in Figure 13) is dipping westwards from the boundary of the EC and SB, with its leading edge to the southern PN. Low attenuation was inferred for this anomaly previously (Liang et al., 2014). Bianchi et al. (2013) detected a smaller-sized high speed block extending from 67°W to 66°W at 100 km depth beneath the CGC and C7, which could be a part of H5 in our image. We interpret this high speed anomaly H5 as delaminated continental lithosphere, which agrees well with the predicted shape of delaminated blocks in the geodynamic modelling studies (Sobolev & Babeyko, 2005; Sobolev et al., 2006; Currie et al., 2015). Those models predict that delamination initiates at the lateral boundary between weak and strong crust (Krystopowicz & Currie, 2013; Currie et al., 2015; Beck et al., 2015) and the delaminated lithosphere block then sinks into the deep upper mantle (Sobolev et al., 2006), causing the upwelling of asthenosphere. In this interpretation, H5 therefore represents an intermediate stage in the delamination process

667 when the lithospheric block has detached but not yet sunken into the deeper mantle. Back-
668 arc low velocity anomaly C7 (Figure 13) atop of H5 is separated from the volcanic arc by a
669 normal to high speed barrier beneath Antofalla (Götze & Krause, 2002) along 26° S (Figure
670 13f). Low velocities at this location were previously interpreted as Cerro Galan Magma
671 Body (Ward et al., 2017). The removal of the lithosphere by delamination supports the
672 formation of the 'MASH' zone (melting, assimilation, storage and homogenization) near
673 the crust-mantle boundary (Hildreth & Moorbath, 1988; Delph et al., 2017; de Silva, S. L.
674 and Kay, Suzanne M., 2018), which might have led to the formation of the Cerro Galan
675 magma chamber (i.e., C7). South of ∼26.5°S, the high velocity zone reaches much further
676 west (anomaly H6, Figure 13), so we prefer to interpret it as the continental lithosphere
677 of the SP (Bianchi et al., 2013; Beck et al., 2015; Scire, Biryol, et al., 2015). There is no
678 clear break between H6 and the Nazca slab, implying the absence of an actively convecting
679 mantle wedge. There is therefore no indication of ongoing or past delamination near the
680 southern limit of the study region.

681 The difference of the back-arc lithospheric depth structure from the southern AP to
682 the southern PN reveals a cold to warm transition of the backarc lithospheric upper mantle.
683 However, the frontal arc and back-arc low velocity anomalies within the middle crust both
684 in our work and previous work (Ward et al., 2017) reveals a reversed pattern: The crustal
685 magma chambers including APMB (Altiplano-Puna Magma Body, C3), LMB (Lazufre
686 Magma Body, C4), IMB (Incahuasi Magma Body, C5), IBMB (Incapillo-Bonete Magma
687 Body C6) and CGMB (Cerro Galan Magma Body, C7) are associated with silicic volcanics.
688 From north to southm they diminish in size and maximum anomaly strength (Ward et al.,
689 2013, 2014, 2017), indicating a reduction of temperature and magma supply in the crust
690 (Allmendinger & Gubbels, 1996; S. M. Kay & Coira, 2009; Beck et al., 2015; Ward et al.,
691 2017).

692 From the history of the deformation and shortening for the Central Andes, north of
693 24°S, tectonic shortening initiated around 50 Ma but the most intensive phase started at
694 30-25 Ma (Allmendinger & Gubbels, 1996; Sobolev & Babeyko, 2005; Oncken et al., 2006;
695 Garzione et al., 2017) and terminated around 10 Ma (Allmendinger et al., 1997; Oncken et
696 al., 2006). In contrast, beneath the southern PN, tectonic shortening started around 20-15
697 Ma but continued until 1-2 Ma (Allmendinger & Gubbels, 1996; Allmendinger et al., 1997;
698 Oncken et al., 2006; Sobolev et al., 2006; S. M. Kay & Coira, 2009). The intense stages of
699 shortening in the AP and PN are perhaps coeval with the passage of the Juan Fernandez
700 Ridge and flat subduction of the Nazca plate (Yáñez et al., 2001; S. M. Kay & Coira, 2009;

Bello-González et al., 2018). The southward sweep of the Juan Fernandez Ridge and the transition to a flat Nazca slab progressively initiates or at least facilitates (S. M. Kay & Coira, 2009; Liang et al., 2014; Beck et al., 2015) the crustal shortening and thickening, which activates the eclogitization of the lower crust and the weakening of the continental lithosphere from the north to the south. The following re-steepening of the Nazca plate beneath the southern AP around 16-11 Ma, 10-6 Ma for the northern PN and 6-3 Ma for the southern PN (S. M. Kay & Coira, 2009) progressively facilitate the injection of the hot astheosphere beneath the weakened continental lithosphere, thus triggering extensive delamination through fulfilling the critical conditions, such as the presence of thick crust (over 45 km) in the back-arc (Sobolev & Babeyko, 2005; Oncken et al., 2006; Sobolev et al., 2006; Krystopowicz & Currie, 2013; de Silva, S. L. and Kay, Suzanne M., 2018; Ibarra et al., 2019), just as we are observing beneath the southern PN now. The delamination process would be followed by the thickening, heating and partial melting of the felsic part of the crust generating a large topography gradient, which would be then evened out by the following crustal flow (Sobolev et al., 2006; DeCelles et al., 2015; Ibarra et al., 2019), like the flat topography of AP. Finally, thin skinned and simple shear deformation pattern developed in the SA (Allmendinger & Gubbels, 1996; Allmendinger et al., 1997; Sobolev & Babeyko, 2005; Ibarra et al., 2019; Garzione et al., 2017) with the underthrusting of the Brazilian shield beneath the AP during the final stage of the shortening after the delamination, just as the high velocity layer H2 we detected in this work.

The initial time for the delamination beneath southern AP is around 20-12 Ma (Sobolev et al., 2006; Beck et al., 2015), while beneath southern PN is inferred at 6-3 Ma (S. M. Kay et al., 1994; S. M. Kay & Coira, 2009; Beck et al., 2015; de Silva, S. L. and Kay, Suzanne M., 2018), near the time of the eruption of the CGC (CGMB, C7). So for the southern PN, the delamination is probably still in progress with asthenosphere warming the base of the crust and possibly accompanied by the steepening process of the Nazca slab. Additionally, de Silva, S. L. and Kay, Suzanne M. (2018) proposed that the southward migration of Juan Fernandez Ridge on the Nazca plate results in a switch in the styles of the volcanism: from a steady state (possibly andesite-dacite) to the flare-up mode (dominantly large-scale ignimbrites and caldera complexes).

To summarise, we could infer a hotter crust but rather colder back-arc lithosphere beneath the southern AP and northern PN with possible underthrusting of the Brazilian shield from our image. In contrast, the relatively cold crust and hot asthenosphere are accompanied by the delaminated lithospheric block sinking beneath the southern PN. The AP has

undergone tectonic shortening for a few tens of millions of years, once created a gravitationally unstable, overthickened mantle lithosphere, finally resulting in the delamination of the lithosphere 15 million years ago (Sobolev et al., 2006), thus acting as a current 'waning' stage for the lithospheric foundering, while the crust of the southern PN is still being heated or has not been fully warmed up by the upwelling asthenosphere during the delamination (Oncken et al., 2006; Beck et al., 2015; Ward et al., 2017), marking the possible 'waxing' stage of the foundering.

6 Conclusions

In this study, we applied full waveform inversion to investigate the seismic velocity structure beneath the Central Andes from 16°S to 30°S and from the Chilean and Peruvian forearc into the Eastern foreland in Brazil and Argentina. We used 117 earthquakes recorded at 584 stations, which provided 9150 unique ray-paths. The new velocity model reveals a high resolution seismic structure including the crust and upper mantle (the spatial resolution is around 20 km in the crust and 30-40 km in the upper mantle), which allows a better understanding of the variation of dehydration in the mantle wedge and subsequent size of crustal magma bodies. The main features are highlighted in Figure 15 with selected volume contours.

(1) The subducting Nazca slab and the transitions between flat and normal-dip subduction are fully imaged in the onshore region.

(2) Large scale crustal partial melting and the hydrated mantle wedge beneath the volcanic arc are also clearly imaged as low velocity zones. There is a general trend, from north to south, for the magnitude of these anomalies to become smaller, demonstrating a spatial variation from the north to the south but there are local variations on top of this trend.

(2a) Hints for higher hydration of the incoming oceanic crust and lithosphere are identified in offshore low velocity anomalies. These are followed by higher inferred degree of serpentinization in the mantle wedge beneath the south Peru, possibly associated with the subduction of the Nazca Fracture Zone.

(2b) Weaker crustal partial melting and a lower degree of hydration within the mantle wedge beneath the Pica Volcanic Gap from 19.8°S to 21°S are observed just where also intraslab seismicity is reduced compared to the south of this anomalous region. At this

latitude, the Iquique ridge is subducting and seems to reduce (rather than enhance) fluid input into the mantle wedge and crust.

(3) Underthrusting of the leading edge from the Brazilian Shield beneath the southern Altiplano and the westward sinking of the delaminated lithosphere beneath the southern Puna are clearly imaged, while the autochthonous lithosphere still appears to be present in the south of the study region below the Sierras Pampeanas. The southward weakening of the crustal magma reservoirs and the variable shapes of the back-arc lithosphere can be interpreted as delineating different stages of the lithospheric evolution. The transition from the 'waning' to the 'waxing' stages of the lithospheric foundering from the north to the south is confirmed and associated with the southward sweeping of the Juan Fernandez Ridge and the flat subduction.

Appendix A Optimization Scheme

A1 Conjugate-Gradients (CG)

We take advantage of the CG variant introduced by Fletcher and Reeves (1964), which has previously been applied to FWI by (Tao et al., 2018). The specific formulation of F-R CG in our study follows as below:

$$\mathbf{z}_i = -\mathbf{G}\mathbf{g}_i + \gamma \mathbf{z}_{i-1} \tag{A1}$$

where $\mathbf{z}_i$ and $\mathbf{z}_{i-1}$ denote the search directions in the ith and $i-1$th iterations, respectively. $\mathbf{g}_i$ is the gradient from the adjoint simulations based on the misfit functions in the ith iteration, $\mathbf{G}$ denotes the smoothing function which contains local (smoothing around the earthquake sources) and global Gaussian smoothing to suppress the local artifacts and stabilize the inversion process. Practically and specifically, for the individual gradient from every event, we use a limited width for the Gaussian smoothing (around 80 km) to damp out artifacts around the sources before summation over all events; we and then clip extreme values of the summed gradients in the shallow crust in order to reduce the artefacts beneath the receivers. The summed gradient is then smoothed again, where the Gaussian smoothing width σ is decreased systematically with each stage of the multi-frequency inversion. Specifically, we set σ equal to one third to one half of the minimum wavelength in the current period. Meanwhile, $\gamma = \frac{(\mathbf{G}\mathbf{g}_i - \mathbf{G}\mathbf{g}_{i-1})^T \mathbf{G}\mathbf{g}_i}{(\mathbf{G}\mathbf{g}_i - \mathbf{G}\mathbf{g}_{i-1})^T \mathbf{z}_{i-1}}$ is the CG update parameter, which is reset to zero when it becomes negative (Tao et al., 2018). The step length for the model updates is determined using a quadratic interpolation among the three test models, which are updated

from the current model with step lengths with 5%, 10% and 15% of the maximum absolute amplitude of the search direction $\mathbf{z}_i$.

A2 L-BFGS

L-BFGS is a quasi-Newton algorithm that contains the curvature information based on the inverse Hessian approximations derived from the gradients and models of the previous iterations and therefore can accelerate convergence. L-BFGS avoids the storage of the very large Hessian matrix and only requires a few vector products. We adopt the methodology from Krischer et al. (2018), which is different from the classical algorithm dating back to D. Liu and Nocedal (1989) by incorporating the Gaussian smoothing operator directly into L-BFGS.

Based on the changes of the gradients defined by $\mathbf{r}_k$=$\mathbf{G}_{1/2}\mathbf{g}_{k+1}$-$\mathbf{G}_{1/2}\mathbf{g}_k$ and the model variations $\mathbf{s}_k$=$\mathbf{m}_{k+1}$-$\mathbf{m}_k$, the L-BFGS is formulated and driven as an iterative algorithm without forming the inverse Hessian approximation directly. The specific algorithm is shown as Algorithm 1.

Algorithm 1 L-BFGS algorithm

$\mathbf{q} \leftarrow \mathbf{G}_{1/2}\mathbf{g}_k$

for $i = k-1, ..., k-m$ **do**

$\gamma_i \leftarrow \frac{1}{\mathbf{r}_i^T\mathbf{s}_i}$; $\alpha_i \leftarrow \gamma_i \mathbf{s}_i^T\mathbf{q}$; $\mathbf{q} \leftarrow \mathbf{q} - \alpha_i\mathbf{r}_i$

end for

$\eta_k \leftarrow (\mathbf{s}_{k-1}^T\mathbf{r}_{k-1})/(\mathbf{r}_{k-1}^T\mathbf{r}_{k-1})$

$\mathbf{z} \leftarrow \eta_k\mathbf{q}$

for $i = k-m, ..., k-1$ **do**

$\beta_i \leftarrow \gamma_i\mathbf{r}_i^T\mathbf{z}$; $\mathbf{z} \leftarrow \mathbf{z} + \mathbf{s}_i(\alpha_i - \beta_i)$

end for

m in the L-BFGS algorithm indicates the number of past model updates stored. In practice, history of the past 6 iterations would be used for every inversion stage once m exceeds 6. The negative direction for the model updates would turn to be $\mathbf{G}_{1/2}\mathbf{z}$=$\mathbf{G}_{1/2}\mathbf{H}_k^{-1}\mathbf{G}_{1/2}\mathbf{g}_k$, where $\mathbf{G}$ is still the smoothing function which is split into $\mathbf{G} = \mathbf{G}_{1/2}\mathbf{G}_{1/2}^T$. So the model update would be:

$$\mathbf{m}_{k+1} = \mathbf{m}_k - \varphi\mathbf{G}_{1/2}\mathbf{z} \tag{A2}$$

where φ represents the suitable step length. In our implementation, we estimate the optimal step length through the quadratic interpolation based on the waveform misfits of three updated test models with φ=20%, 50% and 80%. In practice, instead of calculating the full misfits for the step length tests, we extract 6 - 10 events with the gradient angle smaller than $1/3\pi$ between the individual event gradient and the summed gradient (van Herwaarden et al., 2020) from the current model. The number of the seismic stations for these events should be larger than the average (40 stations) to be representative of the summed gradient. Through this way, we could substantially lower the computational burden for the step length tests and thus improve the efficiency of the inversion.

Acknowledgments

We gratefully acknowledge fruitful discussions with Christian Sippl, Michael Pons, Wei Li, Kevin M. Ward, Nienke Blom, Deborah Wehner, Lion Krischer, Michael Afanasiev and Christian Boehm. This work was supported by the Swiss National Supercomputing Center (CSCS) in the form of computing time grants s961 and s868. Waveform data and station meta data were downloaded using the ObsPy (Krischer, Tobias, et al., 2015) module through the International Federation of Digital Seismograph Networks (FDSN) webservices from multiple data centres. The velocity model would be available for download at IRIS Earth Model Collaboration (EMC) after the paper is accepted. Yajian Gao is also sponsored by Freie Universität Berlin - China Scholarship Council Program and European Cooperation in Science and Technology, Time-Dependent Seismology, Short Term Scientific Missions (STSM); Dirk-Philip van Herwaarden and Solvi Thrastarson were supported by the European Research Council (ERC) under the EU's Horizon 2020 programme (grant No. 714069).

References

Afanasiev, M., Boehm, C., Van Driel, M., Krischer, L., Rietmann, M., May, D. A., ... Fichtner, A. (2019). Modular and flexible spectral-element waveform modelling in two and three dimensions. *Geophysical Journal International*, *216*(3), 1675–1692. doi: https://doi.org/10.1093/gji/ggy469

Albuquerque Seismological Laboratory (ASL)/USGS. (1988). *Global Seismograph Network (GSN - IRIS/USGS).* International Federation of Digital Seismograph Networks. doi: 10.7914/SN/IU

Albuquerque Seismological Laboratory (ASL)/USGS. (1993). *Global Telemetered Seismograph Network (USAF/USGS).* International Federation of Digital Seismograph

Networks. doi: 10.7914/SN/GT

Allmendinger, R. W., & Gubbels, T. (1996). Pure and simple shear plateau uplift, Altiplano-Puna, Argentina and Bolivia. *Tectonophysics*, *259*(1-3 SPEC. ISS.), 1–13. doi: https://doi.org/10.1016/0040-1951(96)00024-8

Allmendinger, R. W., Jordan, T. E., Kay, S. M., & Isacks, B. L. (1997). The evolution of the Altiplano-Puna plateau of the Central Andes. *Annual Review of Earth and Planetary Sciences*, *25*, 139–174. doi: https://doi.org/10.1146/annurev.earth.25.1.139

Amante, C., & Eakins, B. (2009). ETOPO1 1 Arc-Minute Global Relief Model: Procedures, Data Sources and Analysis. *NOAA Technical Memorandum NESDIS NGDC-24*(March), 19. doi: https://doi.org/10.1594/PANGAEA.769615

Angermann, D., Klotz, J., & Reigber, C. (1999). Space-geodetic estimation of the Nazca-South America Euler vector. *Earth and Planetary Science Letters*, *171*(3), 329–334. doi: https://doi.org/10.1016/S0012-821X(99)00173-9

Antonijevic, S. K., Wagner, L. S., Beck, S. L., Long, M. D., Zandt, G., & Tavera, H. (2016). Effects of change in slab geometry on the mantle flow and slab fabric in Southern Peru. *Journal of Geophysical Research: Solid Earth*, *121*(10), 7252-7270. doi: https://doi.org/10.1002/2016JB013064

Antonijevic, S. K., Wagner, L. S., Kumar, A., Beck, S. L., Long, M. D., Zandt, G., ... Condori, C. (2015). The role of ridges in the formation and longevity of flat slabs. *Nature*, *524*(7564), 212–215. doi: 10.1038/nature14648

Araya Vargas, J., Meqbel, N., Ritter, O., Brasse, H., Weckmann, U., Yáñez, G., & Godoy, B. (2019). Fluid distribution in the Central Andes subduction zone imaged with magnetotellurics. *Journal of Geophysical Research: Solid Earth*, *124*(4), 4017–4034.

Asch, G., Heit, B., & Yuan, X. (2002). The ReFuCA project: Receiver Functions Central Andes.

Asch, G., Tilmann, F., Heit, B., & Schurr, B. (2014). HART-PISAGUA Project Chile. doi: 10.14470/8Q7569558037

Asch, G., Tilmann, F., Schurr, B., & Ryberg, T. (2011). Seismic network 5E: MINAS project (2011/2013).

Beck, L., Susan, & Zandt, G. (2002). The nature of orogenic crust in the central Andes. *Journal of Geophysical Research: Solid Earth*, *107*(B10), ESE–7.

Beck, L., Susan, & Zandt, G. (2007). Lithospheric structure and deformation of the flat slab region of Argentina. *International Federation of Digital Seismograph Networks. Dataset/Seismic Network. doi*, *10*.

Beck, L., Susan, Zandt, G., & Wagner, L. (2010). Central Andean uplift and the geodynamics of the high topography. *Other/Seismic Network, International Federation of Digital Seismograph Networks, doi*, *10*.

Beck, L., Susan, Zandt, G., Ward, K. M., & Scire, A. (2015). Multiple styles and scales of lithospheric foundering beneath the Puna Plateau, Central Andes. In *Geodynamics of a Cordilleran Orogenic System: The Central Andes of Argentina and Northern Chile.* Geological Society of America. doi: https://doi.org/10.1130/2015.1212(03)

Bello-González, J. P., Contreras-Reyes, E., & Arriagada, C. (2018). Predicted path for hotspot tracks off South America since Paleocene times: Tectonic implications of ridge-trench collision along the Andean margin. *Gondwana Research*, *64*, 216–234. doi: https://doi.org/10.1016/j.gr.2018.07.008

Bianchi, M., Heit, B., Jakovlev, A., Yuan, X., Kay, S., Sandvol, E., ... Comte, D. (2013). Teleseismic tomography of the southern Puna plateau in Argentina and adjacent regions. *Tectonophysics*, *586*, 65 - 83. doi: https://doi.org/10.1016/j.tecto.2012.11.016

Bishop, B. T., Beck, S. L., Zandt, G., Wagner, L., Long, M., Antonijevic, S. K., ... Tavera, H. (2017). Causes and consequences of flat-slab subduction in southern Peru. *Geosphere*, *13*(5), 1392-1407. doi: https://doi.org/10.1130/GES01440.1

Bjørnerud, M., Austrheim, H., & Lund, M. (2002). Processes leading to eclogitization (densification) of subducted and tectonically buried crust. *Journal of Geophysical Research: Solid Earth*, *107*(B10), ETG–14.

Bloch, W., Kummerow, J., Salazar, P., Wigger, P., & Shapiro, S. A. (2014). High-resolution image of the North Chilean subduction zone: seismicity, reflectivity and fluids. *Geophysical Journal International*, *197*(3), 1744-1749. doi: https://doi.org/10.1093/gji/ggu084

Blom, N., Boehm, C., & Fichtner, A. (2017). Synthetic inversions for density using seismic and gravity data. *Geophysical Journal International*, *209*(2), 1204-1220. doi: https://doi.org/10.1093/gji/ggx076

Blom, N., Gokhberg, A., & Fichtner, A. (2020). Seismic waveform tomography of the central and eastern Mediterranean upper mantle. *Solid Earth*, *11*(2), 669–690. doi: https://doi.org/10.5194/se-11-669-2020

Bunks, C., Saleck, F. M., Zaleski, S., & Chavent, G. (1995). Multiscale seismic waveform inversion. *Geophysics*, *60*(5), 1457–1473.

Calixto, F. J., Sandvol, E., Kay, S., Mulcahy, P., Heit, B., Yuan, X., ... Alvarado, P. (2013). Velocity structure beneath the southern Puna plateau: Evidence for delamination. *Geochemistry, Geophysics, Geosystems*, *14*(10), 4292-4305. doi: https://doi.org/10

.1002/ggge.20266

Cesca, S., Sobiesiak, M., Tassara, A., Olcay, M., Günther, E., Mikulla, S., & Dahm, T. (2009). The Iquique Local Network and PicArray. doi: 10.14470/VD070092

Chen, J., Kufner, S. K., Yuan, X., Heit, B., Wu, H., Yang, D., ... Kay, S. (2020). Lithospheric Delamination Beneath the Southern Puna Plateau Resolved by Local Earthquake Tomography. *Journal of Geophysical Research: Solid Earth*, *125*(10). doi: https://doi.org/10.1029/2019JB019040

Chen, M., Niu, F., Liu, Q., Tromp, J., & Zheng, X. (2015). Multiparameter adjoint tomography of the crust and upper mantle beneath East Asia: 1. Model construction and comparisons. *Journal of Geophysical Research: Solid Earth*, *120*(3), 1762-1786. doi: https://doi.org/10.1002/2014JB011638

Chen, P., Zhao, L., & Jordan, T. H. (2007). Full 3D tomography for the crustal structure of the Los Angeles region. *Bulletin of the Seismological Society of America*, *97*(4), 1094–1120.

Chen, Y., Wu, J., & Suppe, J. (2019). Southward propagation of Nazca subduction along the Andes. *Nature*, *565*(7740), 441–447.

Colli, L., Fichtner, A., & Bunge, H.-P. (2013). Full waveform tomography of the upper mantle in the South Atlantic region: Imaging a westward fluxing shallow asthenosphere? *Tectonophysics*, *604*, 26 - 40. doi: https://doi.org/10.1016/j.tecto.2013.06.015

Comte, D., Carrizo, D., Roecker, S., Ortega-Culaciati, F., & Peyrat, S. (2016). Three-dimensional elastic wave speeds in the northern Chile subduction zone: variations in hydration in the supraslab mantle. *Geophysical Journal International*, *207*(2), 1080-1105. doi: https://doi.org/10.1093/gji/ggw318

Currie, C. A., Ducea, M. N., DeCelles, P. G., & Beaumont, C. (2015). Geodynamic models of Cordilleran orogens: Gravitational instability of magmatic arc roots. *Memoir of the Geological Society of America*, *212*(01), 1–22. doi: https://doi.org/10.1130/2015.1212(01)

de Silva, S. L. (1989). Altiplano-Puna volcanic complex of the central Andes. *Geology*, *17*(12), 1102–1106.

de Silva, S. L. and Kay, Suzanne M. (2018). Turning up the heat: High-flux magmatism in the central andes. *Elements*, *14*(4), 245–250. doi: https://doi.org/10.2138/gselements.14.4.245

DeCelles, P. G., Zandt, G., Beck, S. L., Currie, C. A., Ducea, M. N., Kapp, P., ... Schoenbohm, L. M. (2015). Cyclical orogenic processes in the Cenozoic cen-

tral Andes. *Memoir of the Geological Society of America*, *212*(22), 459–490. doi: https://doi.org/10.1130/2015.1212(22)

Delph, J. R., Ward, K. M., Zandt, G., Ducea, M. N., & Beck, S. L. (2017). Imaging a magma plumbing system from MASH zone to magma reservoir. *Earth and Planetary Science Letters*, *457*, 313 - 324. doi: https://doi.org/10.1016/j.epsl.2016.10.008

Dziewonski, A. M., & Anderson, D. L. (1981). Preliminary reference earth model. *Physics of the Earth and Planetary Interiors*, *25*(4), 297 - 356. doi: https://doi.org/10.1016/0031-9201(81)90046-7

Ekström, G., Nettles, M., & Dziewoński, A. (2012). The global CMT project 2004–2010: Centroid-moment tensors for 13,017 earthquakes. *Physics of the Earth and Planetary Interiors*, *200-201*, 1 - 9. doi: https://doi.org/10.1016/j.pepi.2012.04.002

Ferrand, T. P., Hilairet, N., Incel, S., Deldicque, D., Labrousse, L., Gasc, J., ... Schubnel, A. (2017, 15). Dehydration-driven stress transfer triggers intermediate-depth earthquakes. *Nature Communications*, *8*(1), 15247. doi: 10.1038/ncomms15247

Fichtner, A. (2010). *Full seismic waveform modelling and inversion*. Springer Science & Business Media.

Fichtner, A., Kennett, B. L., Igel, H., & Bunge, H.-P. (2008). Theoretical background for continental and global scale full-waveform inversion in the time–frequency domain. *Geophysical Journal International*, *175*(2), 665–685.

Fichtner, A., Kennett, B. L., Igel, H., & Bunge, H.-P. (2010). Full waveform tomography for radially anisotropic structure: new insights into present and past states of the Australasian upper mantle. *Earth and Planetary Science Letters*, *290*(3-4), 270–280.

Fichtner, A., Kennett, B. L. N., Igel, H., & Bunge, H.-P. (2009). Full seismic waveform tomography for upper-mantle structure in the australasian region using adjoint methods. *Geophysical Journal International*, *179*(3), 1703-1725. doi: https://doi.org/10.1111/j.1365-246X.2009.04368.x

Fichtner, A., & Leeuwen, T. v. (2015). Resolution analysis by random probing. *Journal of Geophysical Research: Solid Earth*, *120*(8), 5549-5573. doi: https://doi.org/10.1002/2015JB012106

Fichtner, A., & Trampert, J. (2011). Resolution analysis in full waveform inversion. *Geophysical Journal International*, *187*(3), 1604–1624.

Fichtner, A., van Herwaarden, D.-P., Afanasiev, M., Simutė, S., Krischer, L., Çubuk Sabuncu, Y., ... Igel, H. (2018). The collaborative seismic earth model: Generation 1. *Geophysical Research Letters*, *45*(9), 4007-4016. doi: https://doi.org/10.1029/2018GL077338

Fletcher, R., & Reeves, C. M. (1964). Function minimization by conjugate gradients. *The Computer Journal*, *7*(2), 149-154. doi: https://doi.org/10.1093/comjnl/7.2.149

Garzione, C. N., McQuarrie, N., Perez, N. D., Ehlers, T. A., Beck, S. L., Kar, N., ... others (2017). Tectonic evolution of the Central Andean plateau and implications for the growth of plateaus. *Annual Review of Earth and Planetary Sciences*, *45*, 529–559.

Garzione, C. N., Molnar, P., Libarkin, J. C., & MacFadden, B. J. (2006). Rapid late Miocene rise of the Bolivian Altiplano: Evidence for removal of mantle lithosphere. *Earth and Planetary Science Letters*, *241*(3-4), 543–556.

GEOFON Data Centre. (1993). *GEOFON Seismic Network.* Deutsches GeoForschungsZentrum GFZ. doi: 10.14470/TR560404

GFZ German Research Centre For Geosciences, & Institut Des Sciences De L'Univers-Centre National De La Recherche CNRS-INSU. (2006). *IPOC Seismic Network.* IPOC Seismic Network, Integrated Plate boundary Observatory Chile - IPOC. doi: 10 .14470/PK615318

Götze, H.-J., & Krause, S. (2002). The Central Andean gravity high, a relic of an old subduction complex? *Journal of South American Earth Sciences*, *14*(8), 799 - 811. doi: https://doi.org/10.1016/S0895-9811(01)00077-3

Hacker, B. R., Peacock, S. M., Abers, G. A., & Holloway, S. D. (2003). Subduction factory 2. Are intermediate-depth earthquakes in subducting slabs linked to metamorphic dehydration reactions? *Journal of Geophysical Research: Solid Earth*, *108*(B1). doi: https://doi.org/10.1029/2001JB001129

Hayes, G. P., Moore, G. L., Portner, D. E., Hearne, M., Flamme, H., Furtney, M., & Smoczyk, G. M. (2018). Slab2, a comprehensive subduction zone geometry model. *Science*, *362*(6410), 58–61. doi: https://doi.org/10.1126/science.aat4723

Heit, B., Bianchi, M., Yuan, X., Kay, S., Sandvol, E., Kumar, P., ... Comte, D. (2014). Structure of the crust and the lithosphere beneath the southern Puna plateau from teleseismic receiver functions. *Earth and Planetary Science Letters*, *385*, 1 - 11. doi: https://doi.org/10.1016/j.epsl.2013.10.017

Heit, B., Koulakov, I., Asch, G., Yuan, X., Kind, R., Alcocer-Rodriguez, I., ... Wilke, H. (2008). More constraints to determine the seismic structure beneath the Central Andes at 21°S using teleseismic tomography analysis. *Journal of South American Earth Sciences*, *25*(1), 22 - 36.

Heit, B., Sodoudi, F., Yuan, X., Bianchi, M., & Kind, R. (2007). An S receiver function analysis of the lithospheric structure in South America. *Geophysical Research Letters*, *34*(14). doi: https://doi.org/10.1029/2007GL030317

Heit, B., Yuan, X., Kind, R., & Asch, G. (2007). Lithospheric dynamics in the southernmost Andean Plateau (PUDEL).

Hildreth, W., & Moorbath, S. (1988). Crustal contributions to arc magmatism in the Andes of central Chile. *Contributions to mineralogy and petrology*, *98*(4), 455–489.

Huang, Z., Tilmann, F., Comte, D., & Zhao, D. (2019). P Wave Azimuthal Anisotropic Tomography in Northern Chile: Insight Into Deformation in the Subduction Zone. *Journal of Geophysical Research: Solid Earth*, *124*(1), 742–765. doi: https://doi.org/10.1029/2018JB016389

Ibarra, F., Liu, S., Meeßen, C., Prezzi, C., Bott, J., Scheck-Wenderoth, M., ... Strecker, M. (2019). 3D data-derived lithospheric structure of the Central Andes and its implications for deformation: Insights from gravity and geodynamic modelling. *Tectonophysics*, *766*, 453 - 468. doi: https://doi.org/10.1016/j.tecto.2019.06.025

Kay, R. W., & Kay, S. M. (1993). Delamination and delamination magmatism. *Tectonophysics*, *219*(1-3), 177–189.

Kay, S. M., Coira, B., & Viramonte, J. (1994). Young mafic back arc volcanic rocks as indicators of continental lithospheric delamination beneath the Argentine Puna Plateau, central Andes. *Journal of Geophysical Research: Solid Earth*, *99*(B12), 24323–24339. doi: https://doi.org/10.1029/94JB00896

Kay, S. M., & Coira, B. L. (2009). Shallowing and steepening subduction zones, continental lithospheric loss, magmatism, and crustal flow under the Central Andean Altiplano-Puna Plateau. In *Backbone of the Americas: Shallow Subduction, Plateau Uplift, and Ridge and Terrane Collision.* Geological Society of America. doi: https://doi.org/10.1130/2009.1204(11)

Kay, S. M., & Mpodozis, C. (2002). Magmatism as a probe to the Neogene shallowing of the Nazca plate beneath the modern Chilean flat-slab. *Journal of South American Earth Sciences*, *15*(1), 39–57.

Kim, Y., & Clayton, R. W. (2015). Seismic properties of the Nazca oceanic crust in southern Peruvian subduction system. *Earth and Planetary Science Letters*, *429*, 110 - 121. doi: https://doi.org/10.1016/j.epsl.2015.07.055

Koulakov, I., Sobolev, S. V., & Asch, G. (2006). P- and S-velocity images of the lithosphere–asthenosphere system in the Central Andes from local-source tomographic inversion. *Geophysical Journal International*, *167*(1), 106-126. doi: https://doi.org/10.1111/j.1365-246X.2006.02949.x

Krischer, L., Fichtner, A., Boehm, C., & Igel, H. (2018). Automated Large-Scale Full Seismic Waveform Inversion for North America and the North Atlantic. *Journal of*

Geophysical Research: Solid Earth, *123*(7), 5902-5928. doi: https://doi.org/10.1029/2017JB015289

Krischer, L., Fichtner, A., Zukauskaite, S., & Igel, H. (2015). Large Scale Seismic Inversion Framework. *Seismological Research Letters*, *86*(4), 1198–1207. doi: https://doi.org/10.1785/0220140248

Krischer, L., Smith, J., Lei, W., Lefebvre, M., Ruan, Y., de Andrade, E. S., ... Tromp, J. (2016). An adaptable seismic data format. *Geophysical Supplements to the Monthly Notices of the Royal Astronomical Society*, *207*(2), 1003–1011.

Krischer, L., Tobias, M., Robert, B., Moritz, B., Thomas, L., Corentin, C., & Joachim, W. (2015). ObsPy: a bridge for seismology into the scientific Python ecosystem. *Computational Science and Discovery*, *8*(1).

Kristeková, M., Kristek, J., & Moczo, P. (2009). Time-frequency misfit and goodness-of-fit criteria for quantitative comparison of time signals. *Geophysical Journal International*, *178*(2), 813-825. doi: https://doi.org/10.1111/j.1365-246X.2009.04177.x

Krystopowicz, N. J., & Currie, C. A. (2013). Crustal eclogitization and lithosphere delamination in orogens. *Earth and Planetary Science Letters*, *361*, 195–207. doi: https://doi.org/10.1016/j.epsl.2012.09.056

Kumar, A., Wagner, L. S., Beck, S. L., Long, M. D., Zandt, G., Young, B., ... Minaya, E. (2016). Seismicity and state of stress in the central and southern Peruvian flat slab. *Earth and Planetary Science Letters*, *441*, 71 - 80. doi: https://doi.org/10.1016/j.epsl.2016.02.023

Lei, W., Ruan, Y., Bozdağ, E., Peter, D., Lefebvre, M., Komatitsch, D., ... Pugmire, D. (2020). Global adjoint tomography - Model GLAD-M25. *Geophysical Journal International*, *223*(1), 1–21. doi: https://doi.org/10.1093/gji/ggaa253

Liang, X., Sandvol, E., Kay, S., Heit, B., Yuan, X., Mulcahy, P., ... Alvarado, P. (2014). Delamination of southern Puna lithosphere revealed by body wave attenuation tomography. *Journal of Geophysical Research: Solid Earth*, *119*(1), 549–566. doi: https://doi.org/10.1002/2013JB010309

Lim, H., Kim, Y., Clayton, R. W., & Thurber, C. H. (2018). Seismicity and structure of Nazca Plate subduction zone in southern Peru. *Earth and Planetary Science Letters*, *498*, 334 - 347. doi: https://doi.org/10.1016/j.epsl.2018.07.014

Liu, D., & Nocedal, J. (1989). On the limited memory BFGS method for large scale optimization. *Mathematical Programming*, *45*(1), 503–528. doi: 10.1007/BF01589116

Liu, Q., & Tromp, J. (2008). Finite-frequency sensitivity kernels for global seismic wave propagation based upon adjoint methods. *Geophysical Journal International*, *174*(1),

265-286. doi: https://doi.org/10.1111/j.1365-246X.2008.03798.x

Liu, Y., Teng, J., Xu, T., Wang, Y., Liu, Q., & Badal, J. (2017). Robust time-domain full waveform inversion with normalized zero-lag cross-correlation objective function. *Geophysical Journal International*, *209*(1), 106–122.

Lu, Y., Stehly, L., Brossier, R., Paul, A., & Group, A. W. (2020). Imaging Alpine crust using ambient noise wave-equation tomography. *Geophysical Journal International*, *222*(1), 69–85.

Luo, Y., & Schuster, G. T. (1991). Wave-equation traveltime inversion. *Geophysics*, *56*(5), 645–653.

Ma, Y., & Clayton, R. W. (2014). The crust and uppermost mantle structure of Southern Peru from ambient noise and earthquake surface wave analysis. *Earth and Planetary Science Letters*, *395*, 61–70. doi: https://doi.org/10.1016/j.epsl.2014.03.013

Ma, Y., & Clayton, R. W. (2015). Flat slab deformation caused by interplate suction force. *Geophysical Research Letters*, *42*(17), 7064-7072. doi: https://doi.org/10.1002/2015GL065195

Madella, A., Delunel, R., Audin, L., & Schlunegger, F. (2018). Why is there no Coastal Cordillera at the Arica Bend (Western Central Andes)? *Basin Research*, *30*(S1), 248-268. doi: https://doi.org/10.1111/bre.12218

Maggi, A., Tape, C., Chen, M., Chao, D., & Tromp, J. (2009). An automated time-window selection algorithm for seismic tomography. *Geophysical Journal International*, *178*(1), 257–281.

Manea, V. C., Manea, M., Ferrari, L., Orozco-Esquivel, T., Valenzuela, R., Husker, A., & Kostoglodov, V. (2017). A review of the geodynamic evolution of flat slab subduction in Mexico, Peru, and Chile. *Tectonophysics*, *695*, 27–52.

Matzel, E., & Grand, S. P. (2004). The anisotropic seismic structure of the East European platform. *Journal of Geophysical Research: Solid Earth*, *109*(B1). doi: https://doi.org/10.1029/2001JB000623

McQuarrie, N., Horton, B. K., Zandt, G., Beck, S., & DeCelles, P. G. (2005). Lithospheric evolution of the Andean fold–thrust belt, Bolivia, and the origin of the central Andean plateau. *Tectonophysics*, *399*(1), 15 - 37. doi: https://doi.org/10.1016/j.tecto.2004.12.013

Meier, U., Curtis, A., & Trampert, J. (2007). Fully nonlinear inversion of fundamental mode surface waves for a global crustal model, journal = Geophysical Research Letters. , *34*(16). doi: https://doi.org/10.1029/2007GL030989

Müller, R. D., Sdrolias, M., Gaina, C., & Roest, W. R. (2008). Age, spreading rates, and spreading asymmetry of the world's ocean crust. *Geochemistry, Geophysics, Geosystems*, *9*(4). doi: https://doi.org/10.1029/2007GC001743

Norabuena, E. O., Dixon, T. H., Stein, S., & Harrison, C. G. A. (1999). Decelerating Nazca-South America and Nazca-Pacific Plate motions. *Geophysical Research Letters*, *26*(22), 3405–3408. doi: https://doi.org/10.1029/1999GL005394

Nuber, A., Manukyan, E., & Maurer, H. (2016). Ground topography effects on near-surface elastic full waveform inversion. *Geophysical Journal International*, *207*(1), 67-71. doi: https://doi.org/10.1093/gji/ggw267

Okazaki, K., & Hirth, G. (2016). Dehydration of lawsonite could directly trigger earthquakes in subducting oceanic crust. *Nature*, *530*(7588), 81–84.

Oncken, O., Asch, G., Haberland, C., Metchie, J., Sobolev, S., Stiller, M., ... others (2003). Seismic imaging of a convergent continental margin and plateau in the central Andes (Andean Continental Research Project 1996 (ANCORP'96)). *Journal of Geophysical Research: Solid Earth*, *108*(B7).

Oncken, O., Hindle, D., Kley, J., Elger, K., Victor, P., & Schemmann, K. (2006). Deformation of the central Andean upper plate system—Facts, fiction, and constraints for plateau models. In *The andes* (pp. 3–27). Springer.

Panning, M., & Romanowicz, B. (2006). A three-dimensional radially anisotropic model of shear velocity in the whole mantle. *Geophysical Journal International*, *167*(1), 361-379. doi: https://doi.org/10.1111/j.1365-246X.2006.03100.x

Peacock, S. M. (2001). Are the lower planes of double seismic zones caused by serpentine dehydration in subducting oceanic mantle? *Geology*, *29*(4), 299–302.

Perkins, J. P., Ward, K. M., De Silva, S. L., Zandt, G., Beck, S. L., & Finnegan, N. J. (2016). Surface uplift in the Central Andes driven by growth of the Altiplano Puna Magma Body. *Nature Communications*, *7*(1), 1–10.

Płonka, A., Blom, N., & Fichtner, A. (2016). The imprint of crustal density heterogeneities on regional seismic wave propagation. *Solid Earth*, *7*(6), 1591–1608. doi: https://doi.org/10.5194/se-7-1591-2016

Porter, R., Gilbert, H., Zandt, G., Beck, S., Warren, L., Calkins, J., ... Anderson, M. (2012). Shear wave velocities in the Pampean flat-slab region from Rayleigh wave tomography: Implications for slab and upper mantle hydration. *Journal of Geophysical Research B: Solid Earth*, *117*(11), 1–21. doi: https://doi.org/10.1029/2012JB009350

Portner, D. E., & Hayes, G. P. (2018). Incorporating teleseismic tomography data into models of upper mantle slab geometry. *Geophysical Journal International*, *215*(1),

325–332. doi: https://doi.org/10.1093/gji/ggy279

Pritchard, M. (2009). The life cycle of Andean volcanoes: combining space-based and field studies.

Ramos, V. A., & Folguera, A. (2009). Andean flat-slab subduction through time. *Geological Society, London, Special Publications*, *327*(1), 31–54.

Ranero, C. R., & Sallarès, V. (2004). Geophysical evidence for hydration of the crust and mantle of the Nazca plate during bending at the north Chile trench. *Geology*, *32*(7), 549–552.

Ritsema, J., Deuss, A., van Heijst, H. J., & Woodhouse, J. H. (2011). S40RTS: a degree-40 shear-velocity model for the mantle from new Rayleigh wave dispersion, teleseismic traveltime and normal-mode splitting function measurements. *Geophysical Journal International*, *184*(3), 1223-1236. doi: https://doi.org/10.1111/j.1365-246X.2010.04884.x

Ritsema, J., & van Heijst, H.-J. (2002). Constraints on the correlation of P- and S-wave velocity heterogeneity in the mantle from P, PP, PPP and PKPab traveltimes. *Geophysical Journal International*, *149*(2), 482-489. doi: https://doi.org/10.1046/j.1365-246X.2002.01631.x

Ritsema, J., van Heijst, H. J., & Woodhouse, J. H. (1999). Complex shear wave velocity structure imaged beneath africa and iceland. *Science*, *286*(5446), 1925–1928.

Rosenbaum, G., Giles, D., Saxon, M., Betts, P. G., Weinberg, R. F., & Duboz, C. (2005). Subduction of the Nazca Ridge and the Inca Plateau: Insights into the formation of ore deposits in Peru. *Earth and Planetary Science Letters*, *239*(1-2), 18–32. doi: https://doi.org/10.1016/j.epsl.2005.08.003

Ruan, Y., Lei, W., Modrak, R., Örsvuran, R., Bozdağ, E., & Tromp, J. (2019). Balancing unevenly distributed data in seismic tomography: A global adjoint tomography example. *Geophysical Journal International*, *219*(2), 1225–1236. doi: https://doi.org/10.1093/gji/ggz356

Salazar, P., Wigger, P., Bloch, W., Asch, G., Shapiro, S., & Kummerow, J. (2013). MEJIPE, GFZ Data Services, Other/Seismic Network.

Sandvol, E., & Brown, L. (2007). SLIP—Seismic Lithospheric Imaging of the Puna Plateau, doi: 10.7914/SN. *X6_2007*.

Schorlemmer, D., Euchner, F., Kästli, P., & Saul, J. (2011). Quakeml: status of the xml-based seismological data exchange format. *Annals of Geophysics*, *54*(1), 59–65. doi: https://doi.org/10.4401/ag-4874

Schurr, B., Asch, G., Rietbrock, A., Trumbull, R., & Haberland, C. (2003). Complex patterns of fluid and melt transport in the central Andean subduction zone revealed by attenuation tomography. *Earth and Planetary Science Letters*, *215*(1-2), 105–119. doi: 10.1016/S0012-821X(03)00441-2

Schurr, B., Asch, G., & Wigger, P. (1997). *PUNA Project Western Argentina.* GFZ Data Services. doi: doi:10.14470/MO6442843258

Schurr, B., & Rietbrock, A. (2004). Deep seismic structure of the Atacama basin, northern Chile. *Geophysical Research Letters*, *31*(12). doi: https://doi.org/10.1029/2004GL019796

Schurr, B., Rietbrock, A., Asch, G., Kind, R., & Oncken, O. (2006). Evidence for lithospheric detachment in the central Andes from local earthquake tomography. *Tectonophysics*, *415*(1), 203 - 223. doi: https://doi.org/10.1016/j.tecto.2005.12.007

Scire, A., Biryol, C. B., Zandt, G., & Beck, S. (2015). Imaging the nazca slab and surrounding mantle to 700 km depth beneath the central andes (18 s to 28 s). *Geodynamics of a Cordilleran Orogenic System: The Central Andes of Argentina and Northern Chile: Geological Society of America Memoir*, *212*, 23–41.

Scire, A., Zandt, G., Beck, S., Long, M., & Wagner, L. (2017). The deforming Nazca slab in the mantle transition zone and lower mantle: Constraints from teleseismic tomography on the deeply subducted slab between 6°S and 32°S. *Geosphere*, *13*(3), 665-680. doi: https://doi.org/10.1130/GES01436.1

Scire, A., Zandt, G., Beck, S., Long, M., Wagner, L., Minaya, E., & Tavera, H. (2015). Imaging the transition from flat to normal subduction: variations in the structure of the Nazca slab and upper mantle under southern Peru and northwestern Bolivia. *Geophysical Journal International*, *204*(1), 457-479. doi: https://doi.org/10.1093/gji/ggv452

Silver, P., Beck, S., & Wallace, T. (1994). Broadband study of the Altiplano and central Andes.

Simutė, S., Steptoe, H., Cobden, L., Gokhberg, A., & Fichtner, A. (2016). Full-waveform inversion of the Japanese Islands region. *Journal of Geophysical Research: Solid Earth*, *121*(5), 3722-3741. doi: https://doi.org/10.1002/2016JB012802

Sippl, C., Schurr, B., Asch, G., & Kummerow, J. (2018). Seismicity structure of the northern chile forearc from 100,000 double-difference relocated hypocenters. *Journal of Geophysical Research: Solid Earth*, *123*(5), 4063–4087.

Sobiesiak, M., & Schurr, B. (2007). Taskforce Tocopilla 2007.

Sobolev, S. V., & Babeyko, A. Y. (1994). Modeling of mineralogical composition, density and elastic wave velocities in anhydrous magmatic rocks. *Surveys in geophysics*, *15*(5), 515–544.

Sobolev, S. V., & Babeyko, A. Y. (2005). What drives orogeny in the Andes? *Geology*, *33*(8), 617–620. doi: https://doi.org/10.1130/G21557.1

Sobolev, S. V., Babeyko, A. Y., Koulakov, I., & Oncken, O. (2006). Mechanism of the Andean Orogeny: Insight from Numerical Modeling. In O. Oncken et al. (Eds.), *The andes: Active subduction orogeny* (pp. 513–535). Berlin, Heidelberg: Springer Berlin Heidelberg. doi: https://doi.org/10.1007/978-3-540-48684-8_25

Storch, I., Buske, S., Schmelzbach, C., & Wigger, P. (2016). Seismic imaging of a megathrust splay fault in the North Chilean subduction zone (Central Andes). *Tectonophysics*, *689*, 157 - 166. doi: https://doi.org/10.1016/j.tecto.2016.02.039

Tao, K., Grand, S. P., & Niu, F. (2017). Full-waveform inversion of triplicated data using a normalized-correlation-coefficient-based misfit function. *Geophysical Journal International*, *210*(3), 1517-1524. doi: https://doi.org/10.1093/gji/ggx249

Tao, K., Grand, S. P., & Niu, F. (2018). Seismic Structure of the Upper Mantle Beneath Eastern Asia From Full Waveform Seismic Tomography. *Geochemistry, Geophysics, Geosystems*, *19*(8), 2732-2763. doi: https://doi.org/10.1029/2018GC007460

Tape, C., Liu, Q., Maggi, A., & Tromp, J. (2010). Seismic tomography of the southern California crust based on spectral-element and adjoint methods. *Geophysical Journal International*, *180*(1), 433–462.

Tassara, A. (2005). Interaction between the Nazca and South American plates and formation of the Altiplano-Puna plateau: Review of a flexural analysis along the Andean margin (15°-34°S). *Tectonophysics*, *399*, 39–57. doi: https://doi.org/10.1016/j.tecto.2004.12.014

Tassara, A., & Echaurren, A. (2012). Anatomy of the Andean subduction zone: three-dimensional density model upgraded and compared against global-scale models. *Geophysical Journal International*, *189*(1), 161-168. doi: https://doi.org/10.1111/j.1365-246X.2012.05397.x

Thrastarson, S., van Driel, M., Krischer, L., Boehm, C., Afanasiev, M., van Herwaarden, D. P., & Fichtner, A. (2020). Accelerating numerical wave propagation by wavefield adapted meshes. part II: full-waveform inversion. *Geophysical Journal International*, *221*(3), 1591–1604.

Thrastarson, S., van Herwaarden, D. P., Krischer, L., & Fichtner, A. (2021). LASIF: Large-scale Seismic Inversion Framework, an updated version.

doi: 10.31223/x5nc84

Tromp, J., Tape, C., & Liu, Q. (2005). Seismic tomography, adjoint methods, time reversal and banana-doughnut kernels. *Geophysical Journal International*, *160*(1), 195-216. doi: https://doi.org/10.1111/j.1365-246X.2004.02453.x

Universidad De Chile. (2013). Red Sismologica Nacional. doi: 10.7914/SN/C1

van Driel, M., Boehm, C., Krischer, L., & Afanasiev, M. (2020). Accelerating numerical wave propagation using wavefield adapted meshes. Part I: forward and adjoint modelling. *Geophysical Journal International*, *221*(3), 1580–1590.

van Herwaarden, D. P., Afanasiev, M., Thrastarson, S., & Fichtner, A. (2021). Evolutionary full-waveform inversion. *Geophysical Journal International*, *224*(1), 306–311.

van Herwaarden, D. P., Boehm, C., Afanasiev, M., Thrastarson, S., Krischer, L., Trampert, J., & Fichtner, A. (2020). Accelerated full-waveform inversion using dynamic mini-batches. *Geophysical Journal International*, *221*(2), 1427-1438. doi: https://doi.org/10.1093/gji/ggaa079

Venzke, E. (2013). Global volcanism program. *Volcanoes of the World*, *4*, 1.

Victor, P., Oncken, O., & Glodny, J. (2004). Uplift of the western Altiplano plateau: Evidence from the Precordillera between 20° and 21°S (northern Chile). *Tectonics*, *23*(4). doi: https://doi.org/10.1029/2003TC001519

Vilotte, J., et al. (2011). Seismic network XS: CHILE MAULE aftershock temporary experiment (RESIF-SISMOB).

Wagner, L., Beck, S., & Long, M. (2010). Peru lithosphere and slab experiment. *Other/Seismic Network, International Federation of Digital Seismograph Networks*, *10*.

Wagner, L., Caddick, M., Kumar, A., Beck, S., & Long, M. (2020, July 10). Effects of oceanic crustal thickness on intermediate depth seismicity. *Frontiers in Earth Science*. doi: 10.3389/feart.2020.00244

Wang, H., & Currie, C. A. (2015). Magmatic expressions of continental lithosphere removal. *Journal of Geophysical Research: Solid Earth*, *120*(10), 7239–7260.

Ward, K. M., Delph, J. R., Zandt, G., Beck, S. L., & Ducea, M. N. (2017). Magmatic evolution of a Cordilleran flare-up and its role in the creation of silicic crust. *Scientific Reports*, *7*(1), 1–8. doi: https://doi.org/10.1038/s41598-017-09015-5

Ward, K. M., Porter, R. C., Zandt, G., Beck, S. L., Wagner, L. S., Minaya, E., & Tavera, H. (2013). Ambient noise tomography across the Central Andes. *Geophysical Journal International*, *194*(3), 1559-1573. doi: https://doi.org/10.1093/gji/ggt166

Ward, K. M., Zandt, G., Beck, S. L., Christensen, D. H., & McFarlin, H. (2014). Seismic imaging of the magmatic underpinnings beneath the Altiplano-Puna volcanic complex from the joint inversion of surface wave dispersion and receiver functions. *Earth and Planetary Science Letters*, *404*, 43 - 53. doi: https://doi.org/10.1016/j.epsl.2014.07.022

Ward, K. M., Zandt, G., Beck, S. L., Wagner, L. S., & Tavera, H. (2016). Lithospheric structure beneath the northern Central Andean Plateau from the joint inversion of ambient noise and earthquake-generated surface waves. *Journal of Geophysical Research: Solid Earth*, *121*(11), 8217-8238. doi: https://doi.org/10.1002/2016JB013237

West, M., & Christensen, D. (2010). Investigating the relationship between pluton growth and volcanism at two active intrusions in the central Andes: International Federation of Digital Seismograph Networks, Other/Seismic Network. *Other/Seismic Network, http://www. fdsn. org/networks/detail/XP_2010/, doi*, *10*.

Whitman, D., Isacks, B., & Kay, S. (1996). Lithospheric structure and along-strike segmentation of the Central Andean Plateau: seismic Q, magmatism, flexure, topography and tectonics. *Tectonophysics*, *259*(1), 29 - 40. (Geodynamics of The Andes) doi: https://doi.org/10.1016/0040-1951(95)00130-1

Wigger, P., Salazar, P., Kummerow, J., Bloch, W., Asch, G., & Shapiro, S. (2016). West–Fissure- and Atacama-Fault Seismic Network (2005/2012). doi: 10.14470/3S7550699980

Wörner, G., Hammerschmidt, K., Henjes-Kunst, F., Lezaun, J., & Wilke, H. (2000). Geochronology (40Ar/39Ar, K-Ar and He-exposure ages) of Cenozoic magmatic rocks from northern Chile (18-22 S): implications for magmatism and tectonic evolution of the central Andes. *Revista geológica de Chile*, *27*(2), 205–240.

Wörner, G., Moorbath, S., & Harmon, R. S. (1992). Andean cenozoic volcanic centers reflect basement isotopic domains. *Geology*, *20*(12), 1103–1106.

Wölbern, I., Heit, B., Yuan, X., Asch, G., Kind, R., Viramonte, J., ... Wilke, H. (2009). Receiver function images from the Moho and the slab beneath the Altiplano and Puna plateaus in the Central Andes. *Geophysical Journal International*, *177*(1), 296-308. doi: https://doi.org/10.1111/j.1365-246X.2008.04075.x

Xiao, Z., Fuji, N., Iidaka, T., Gao, Y., Sun, X., & Liu, Q. (2020). Seismic Structure Beneath the Tibetan Plateau From Iterative Finite-Frequency Tomography Based on ChinArray: New Insights Into the Indo-Asian Collision. *Journal of Geophysical Research: Solid Earth*, *125*(2). doi: https://doi.org/10.1029/2019JB018344

Yáñez, G. A., Ranero, C. R., Von Huene, R., & Díaz, J. (2001). Magnetic anomaly interpretation across the southern central Andes (32°-34°S): The role of the Juan Fernández Ridge in the late Tertiary evolution of the margin. *Journal of Geophysical Research: Solid Earth*, *106*(B4), 6325–6345. doi: https://doi.org/10.1029/2000jb900337

Yoon, M., Buske, S., Shapiro, S., & Wigger, P. (2009). Reflection Image Spectroscopy across the Andean subduction zone. *Tectonophysics*, *472*(1), 51 - 61. doi: https://doi.org/10.1016/j.tecto.2008.03.014

Yuan, X., Sobolev, S., & Kind, R. (2002). Moho topography in the central Andes and its geodynamic implications. *Earth and Planetary Science Letters*, *199*(3), 389 - 402. doi: https://doi.org/10.1016/S0012-821X(02)00589-7

Yuan, X., Sobolev, S. V., Kind, R., Oncken, O., Bock, G., Asch, G., ... Comte, D. (2000). Subduction and collision processes in the Central Andes constrained by converted seismic phases. *Nature*, *408*(6815), 958-961. doi: 10.1038/35050073

Yuan, Y. O., Bozdağ, E., Ciardelli, C., Gao, F., & Simons, F. J. (2020). The exponentiated phase measurement, and objective-function hybridization for adjoint waveform tomography. *Geophysical Journal International*, *221*(2), 1145–1164.

Zandt, G. (1996). Altiplano-Puna Volcanic Complex Seismic Experiment.

Zhu, H., Bozdăg, E., & Tromp, J. (2015). Seismic structure of the European upper mantle based on adjoint tomography. *Geophysical Journal International*, *201*(1), 18–52. doi: https://doi.org/10.1093/gji/ggu492

Zhu, H., Komatitsch, D., & Tromp, J. (2017). Radial anisotropy of the North American upper mantle based on adjoint tomography with USArray. *Geophysical Journal International*, *211*(1), 349-377. doi: https://doi.org/10.1093/gji/ggx305

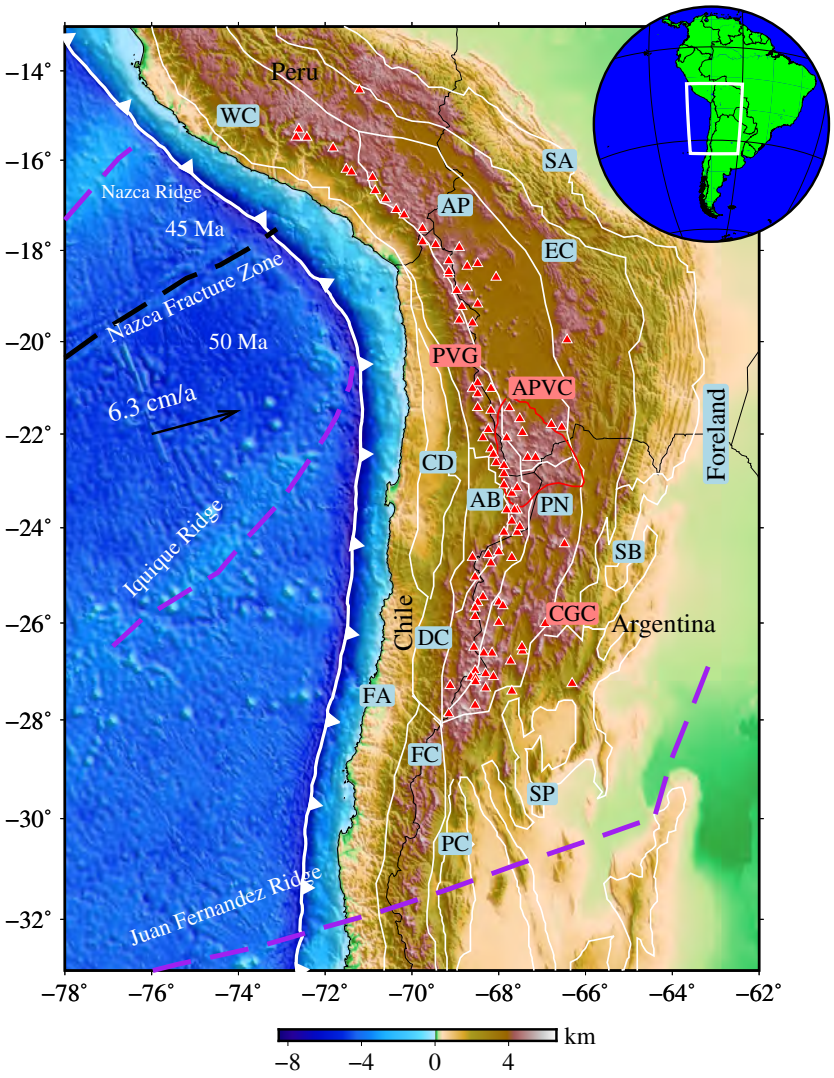

Figure 1. Map of major morphotectonic provinces and volcanism centers (modified from Tassara, 2005) in the Central Andes, including the forearc (FA), Central Depression (CD), Domeyko Cordillera (DC), Atacama Basin(AB), Frontal Cordillera (FC), Western Cordillera (WC), Altiplano (AP), Eastern Cordillera (EC), Puna (PN), Precordillera (PC), Subandean Ranges (SA), Santa Barbara system (SB), Sierras Pampeanas (SP); Altiplano-Puna Volcanic Complex (APVC, enclosed by the red line). Cerro Galan Caldera (CGC); Pica Volcanic Gap (PVG). The purple dashed lines represent three major oceanic Ridges, including the Nazca Ridge, Iquique Ridge and Juan Fernandez Ridge. The reconstruction of the trace of the subducted Juan Fernandez Ridge has been taken from Yáñez et al. (2001). Red triangles denote volcanoes (retrieved from Global Volcanism Program, Smithsonian Institution, Venzke, 2013). Topography data has been retrieved from the ETOPO1 Global Relief Model (Amante & Eakins, 2009); the white saw-tooth line denotes the position of the Trench. Inset marks the position of our study region in South America.

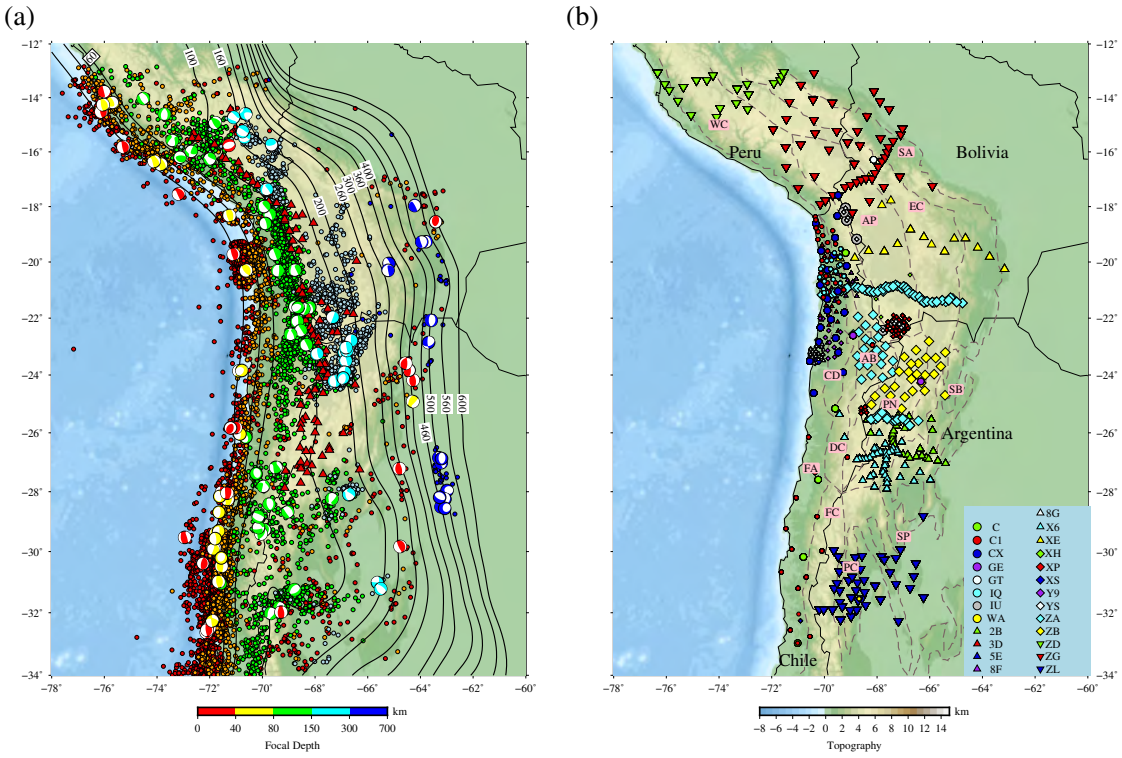

Figure 2. (a) Map showing seismicity (magnitude > Mw 2.5) and Nazca slab depth contours. Black lines represent the slab contours, retrieved from the Slab2.0 global subduction zone model (Hayes et al., 2018), seismicity from 1991 to 2019 was extracted from the U.S. Geological Survey-National Earthquake Information Center (NEIC) catalog (https://earthquake.usgs.gov/earthquakes/search/). The beach balls indicate the focal mechanisms of the earthquakes used for the FWI in this study. (b) Map showing seismic stations of individual networks used in the study with circles marking the permanent stations. Detailed information about the networks is given in Table 1.

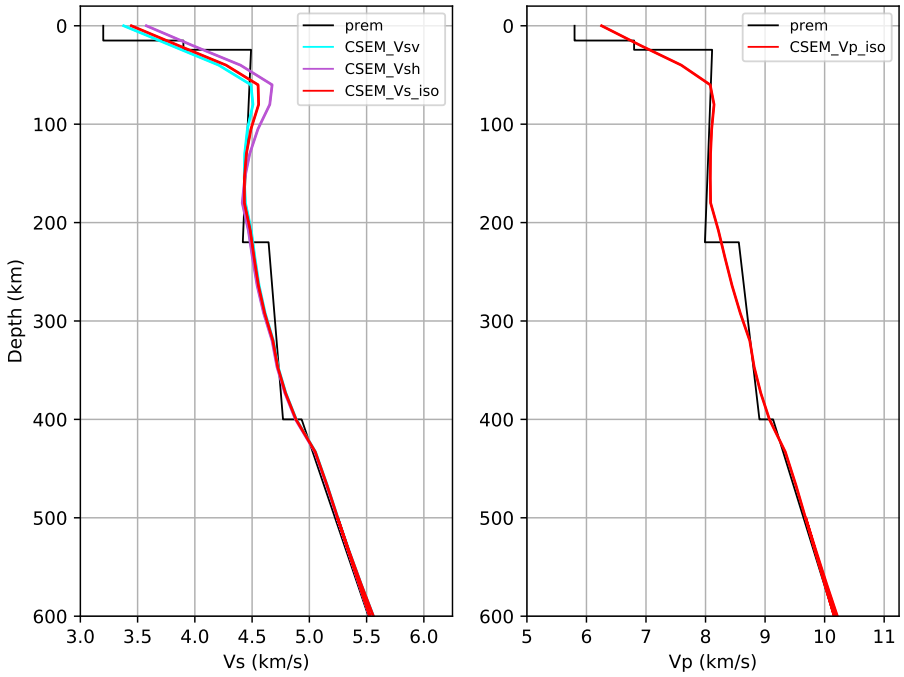

Figure 3. The reference 1D model derived from the depth-averaged initial CSEM model (Fichtner et al., 2018), compared with isotropic PREM (Dziewonski & Anderson, 1981).

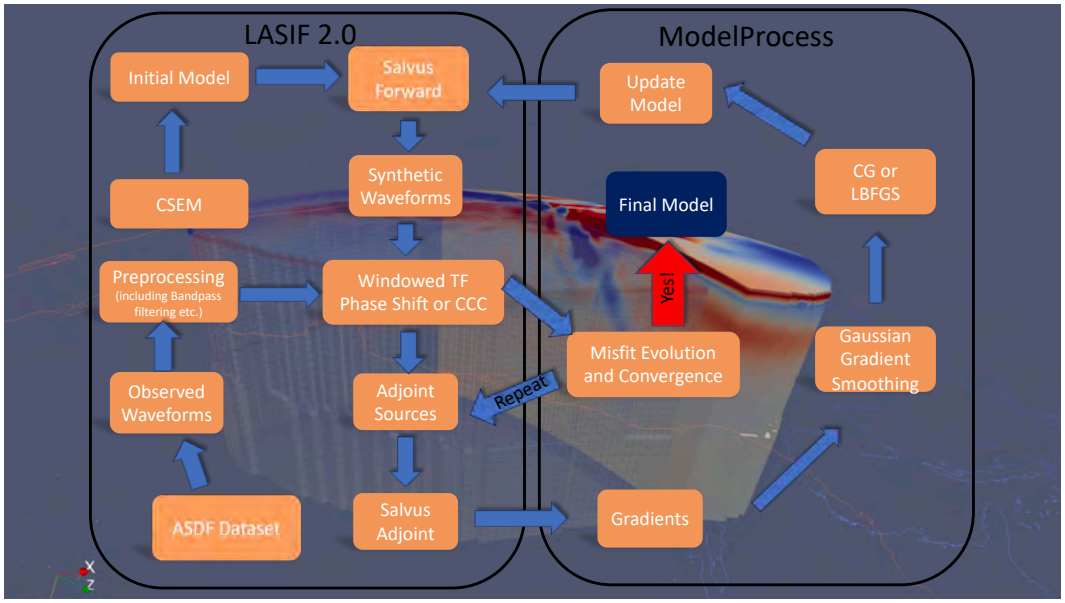

Figure 4. Inversion workflow in this study with Conjugate-Gradient (CG) and L-BFGS implemented. The background is the 3D view of the final V_S velocity model.

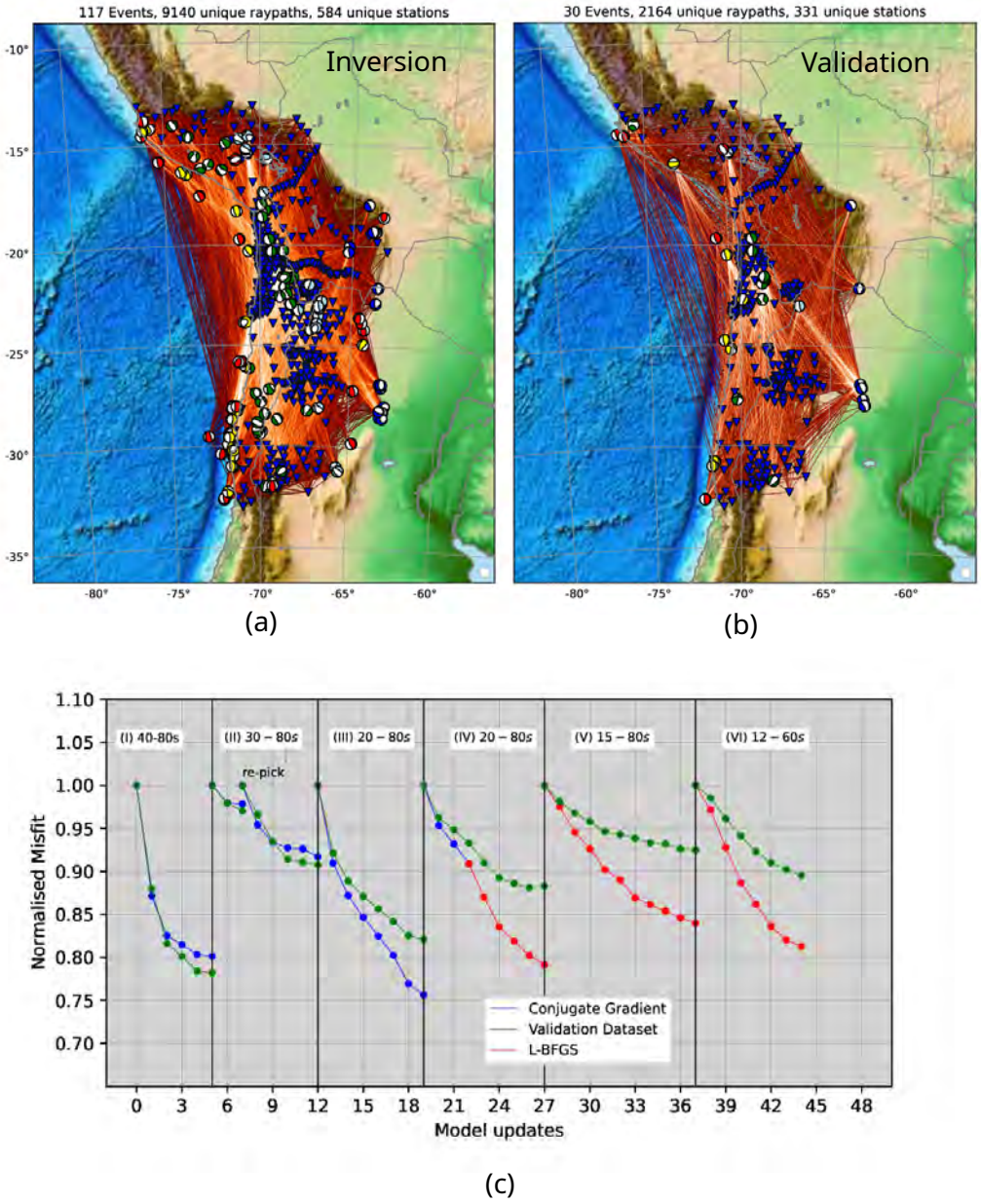

Figure 5. (a) Total ray-paths used for the inversion with earthquakes and stations (b) Ray-path for the validation dataset (c) Misfit evolution over the complete inversion comprising six stages over progressively increasing frequency bands. The blue and red lines denote the misfits evolution using the Conjugate Gradient and L-BFGS method respectively. Misfits are normalised relative to each onset of the individual inversion stages. The green lines indicate the misfit evolution of the validation dataset.

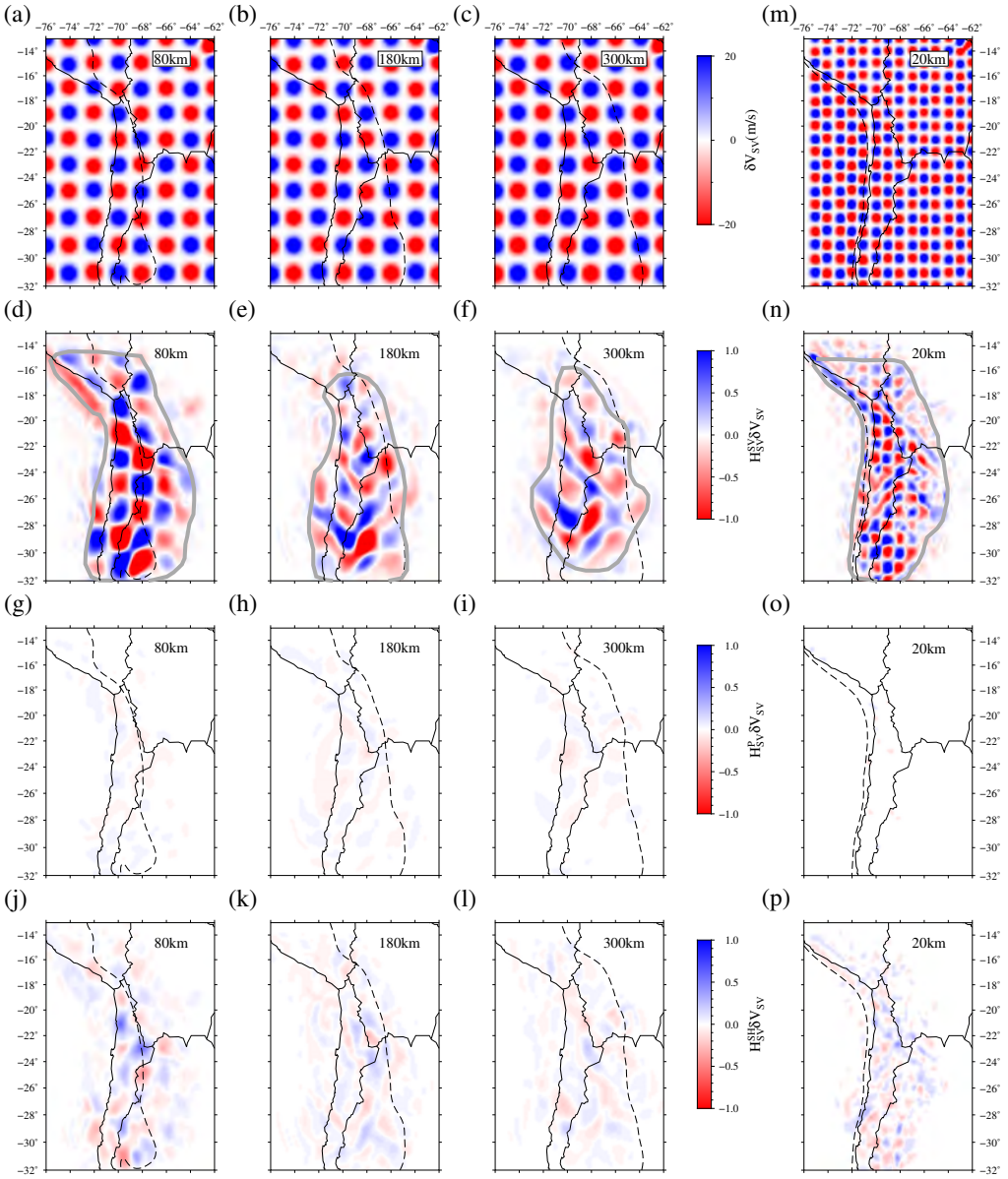

Figure 6. Resolution estimates based on $\mathbf{H}\delta\mathbf{m}$, using the CCC misfit function and the same time windows and model as in the final inversion stage (VI) (see text). (a)-(c): Horizontal slices of input ($\delta\mathbf{m}$) 1% Gaussian $\mathbf{V}_{SV}$ perturbations ($\delta\mathbf{V}_{SV}$) with σ=40 km at 80 km, 180 km and 300 km depth in the upper mantle. (d)-(f): $\mathbf{H}^{SV}_{SV}\delta\mathbf{V}_{SV}$ for the upper mantle with respect to $\mathbf{V}_{SV}$ perturbations ($\delta\mathbf{V}_{SV}$); (g)-(i): $\mathbf{H}^{P}_{SV}\delta\mathbf{V}_{SV}$ for $\mathbf{V}_P$ with respect to $\delta\mathbf{V}_{SV}$, which represents the trade-offs between $\mathbf{V}_{SV}$ and $\mathbf{V}_P$; (j)-(l): Point-spread functions ($\mathbf{H}^{SH}_{SV}\delta\mathbf{V}_{SV}$) for $\mathbf{V}_{SH}$ with respect to $\delta\mathbf{V}_{SV}$, which represents the trade-offs between $\mathbf{V}_{SV}$ and $\mathbf{V}_{SH}$; (m): Independent test for the crust with input $\delta\mathbf{m}$ of 1% Gaussian V_{SV} perturbations ($\delta\mathbf{V}_{SV}$) with σ=25 km at 20 km; (n)-(p): Point-spread functions of $\mathbf{V}_{SV}$, $\mathbf{V}_P$ and $\mathbf{V}_{SH}$ in the crust with respect to the input perturbations of $\delta\mathbf{V}_{SV}$ in (m). The grey lines denote the trust region for the interpretations in Section 5.

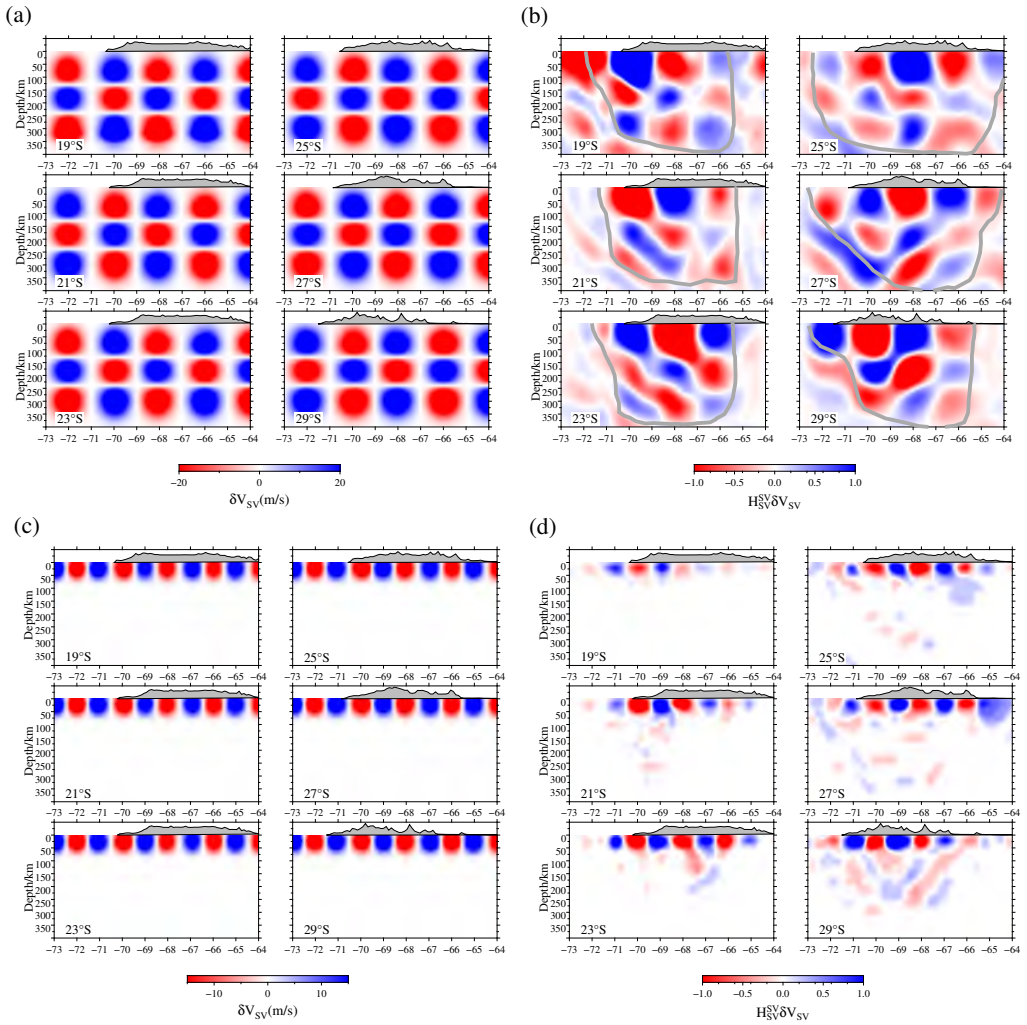

Figure 7. East-west cross-sections of resolution tests for $\mathbf{V}_{SV}$ (see Fig. 6 and text for details) (a): Input $\delta\mathbf{m}$ for the $\mathbf{V}_{SV}$ perturbations ($\delta\mathbf{V}_{SV}$) in the mantle; (b): $\mathbf{H}_{SV}^{SV}\delta\mathbf{V}_{SV}$ in the upper mantle; (c): Input $\delta\mathbf{m}$ of V_{SV} perturbations ($\delta\mathbf{V}_{SV}$) in the crust; (d): $\mathbf{H}_{SV}^{SV}\delta\mathbf{V}_{SV}$ for V_{SV} in the crust.

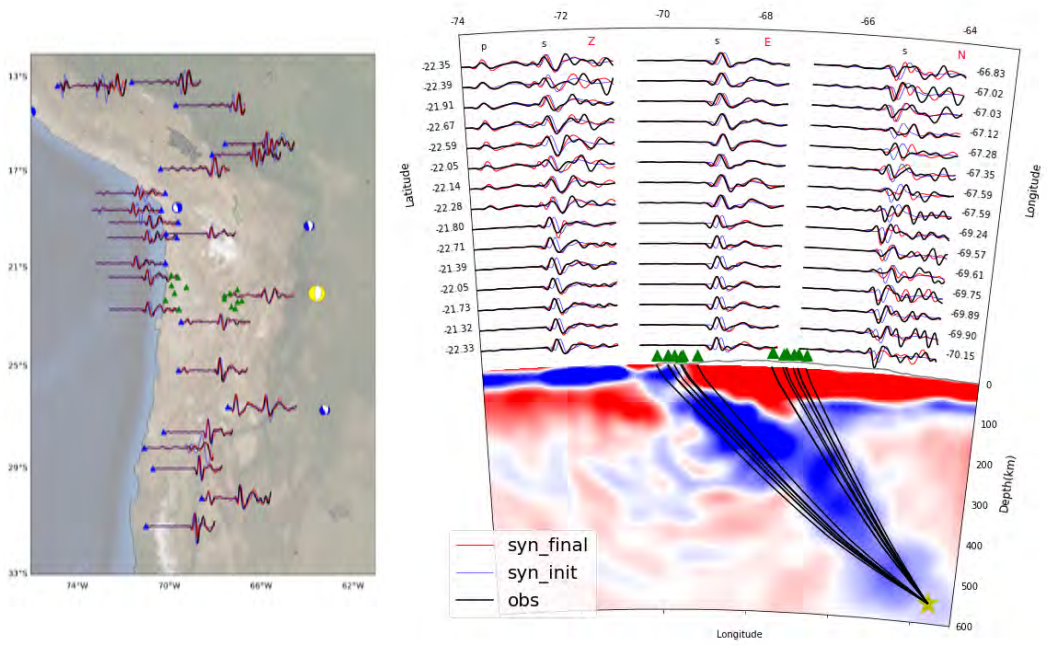

Figure 8. (a): Waveform fits for Z component from the sample events beneath the Central Andes. Blue and red seismograms denote the synthetics from the initial and final models, respectively. Black seismograms represent the observed waveforms. Earthquakes and seismic stations are denoted by beach balls and triangles, respectively; (b): A cross section of the tomography model along 22°S. Black solid lines depict indicative up-going S wave ray paths, calculated based on the 1D PREM Model with the Taup module in Obspy. Three component waveforms in the top panel are arranged by the longitude. Yellow star marks the position of the deep event. The locations in the map of this event and stations are denoted by the yellow beach ball and green triangles in (a).

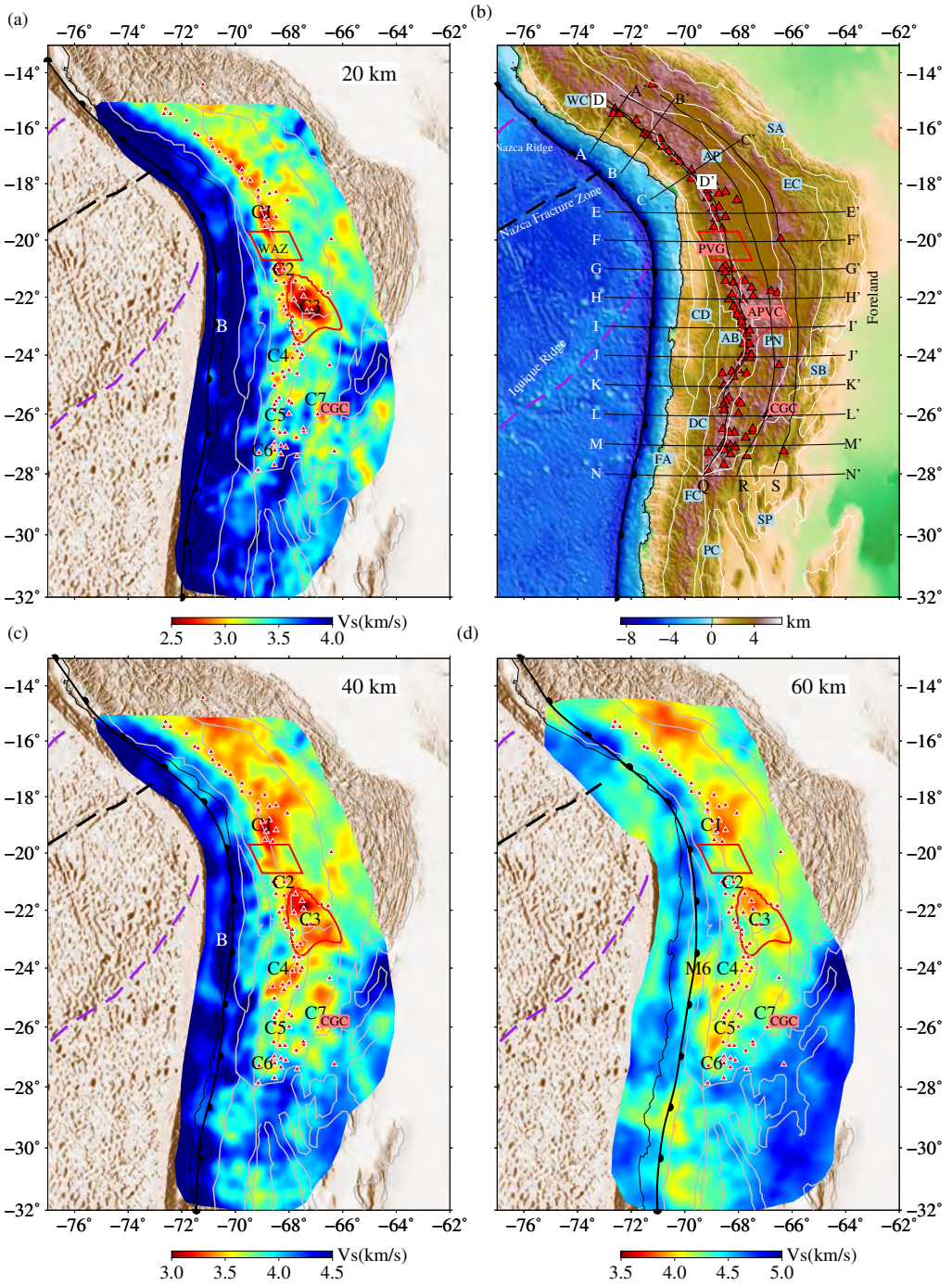

Figure 9. Horizontal slices for the isotropic V_S in the crust at depths of 20 km (a), 40 km (c) and 60 km (d). Thick black lines with tooth denote the slab contours from Slab2.0. (b): Topographic map with the locations of the cross-sections (solid black lines with labels) shown in Figure 11–14. Red box and circle denote the locations of the PVG (WAZ) and APVC, respectively. C1-C7 and B denote the crustal velocity anomalies discussed in the text. Please note that different color scales are used for the different depth levels.

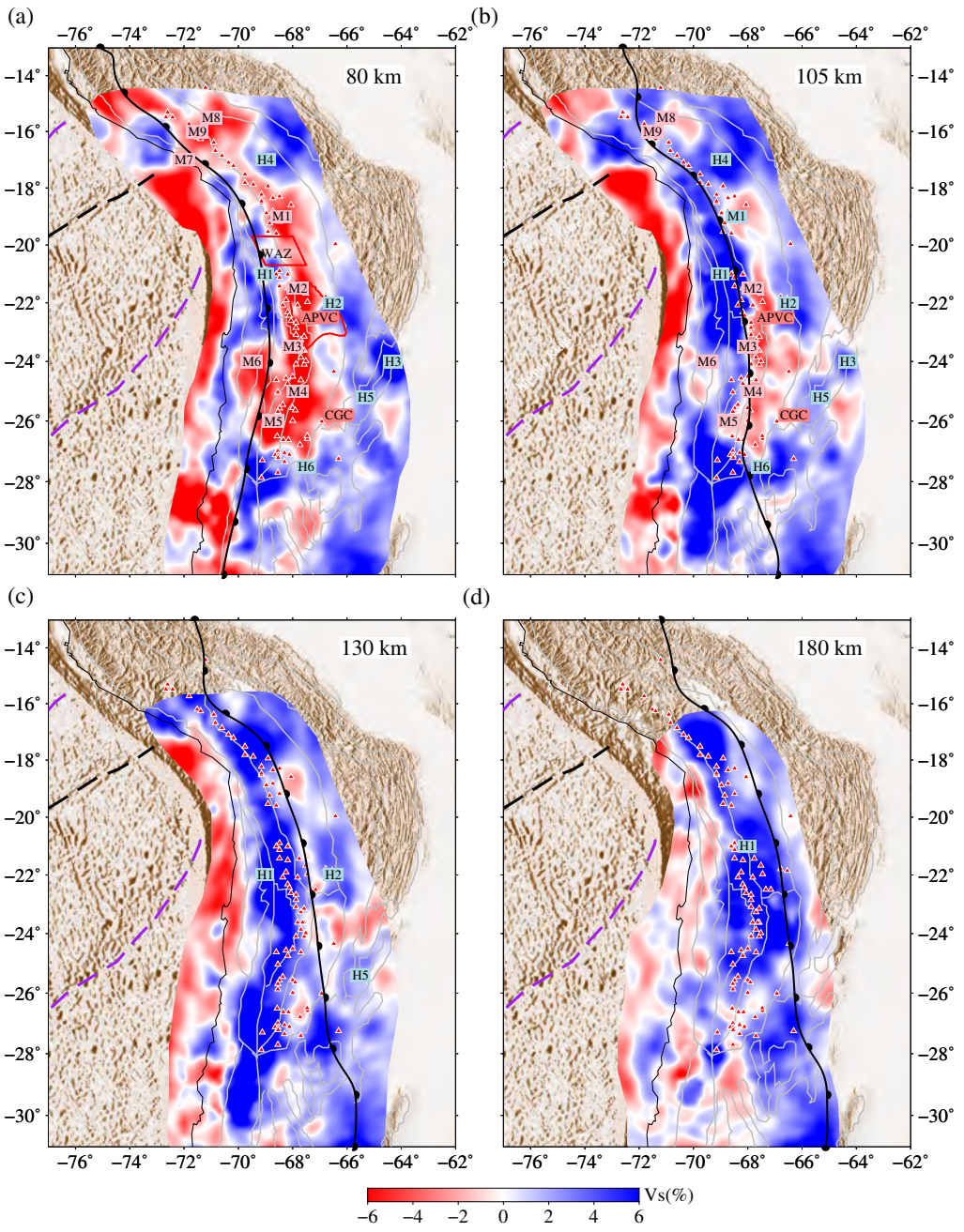

Figure 10. Horizontal slices for the isotropic V_S perturbations for the upper mantle at depths of 80 km (a), 105 km (b), 130 km(c) and 180 km (d). The reference model is the 1D isotropic V_S from the CSEM shown in Figure 3. H1-H6 and M1-M9 indicate the high and low velocity anomalies within the slab and the continental mantle which are used for discussion.

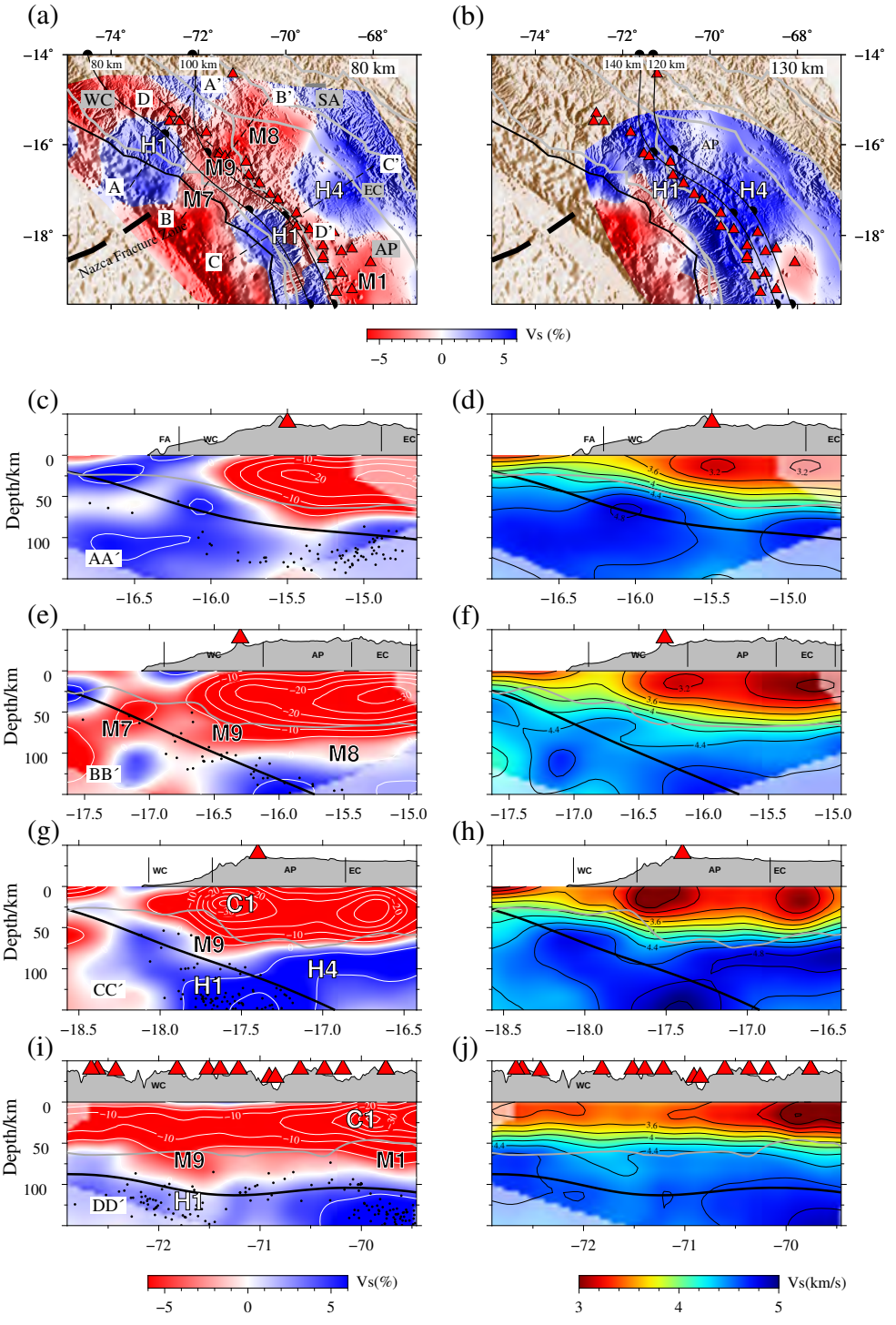

Figure 11. (a) and (b) are zoomed-in horizontal slices for V_S perturbations at depths of 80 and 130 km beneath the southern Peru. Black dashed lines in (a) mark the positions of profile AA' – DD'. (c), (e), (g) and (i) are cross sections of V_S perturbations. Thin white lines mark 5% perturbation contours. (d), (f), (h) and (j) are absolute V_S velocity model. Thin black lines mark 0.2 km/s velocity contours. Solid black lines denote the slab contours from Slab 2.0 and the solid dark grey lines indicate the Moho depth extracted from Bishop et al. (2017). The black dots are seismicity retrieved from Kumar et al. (2016).

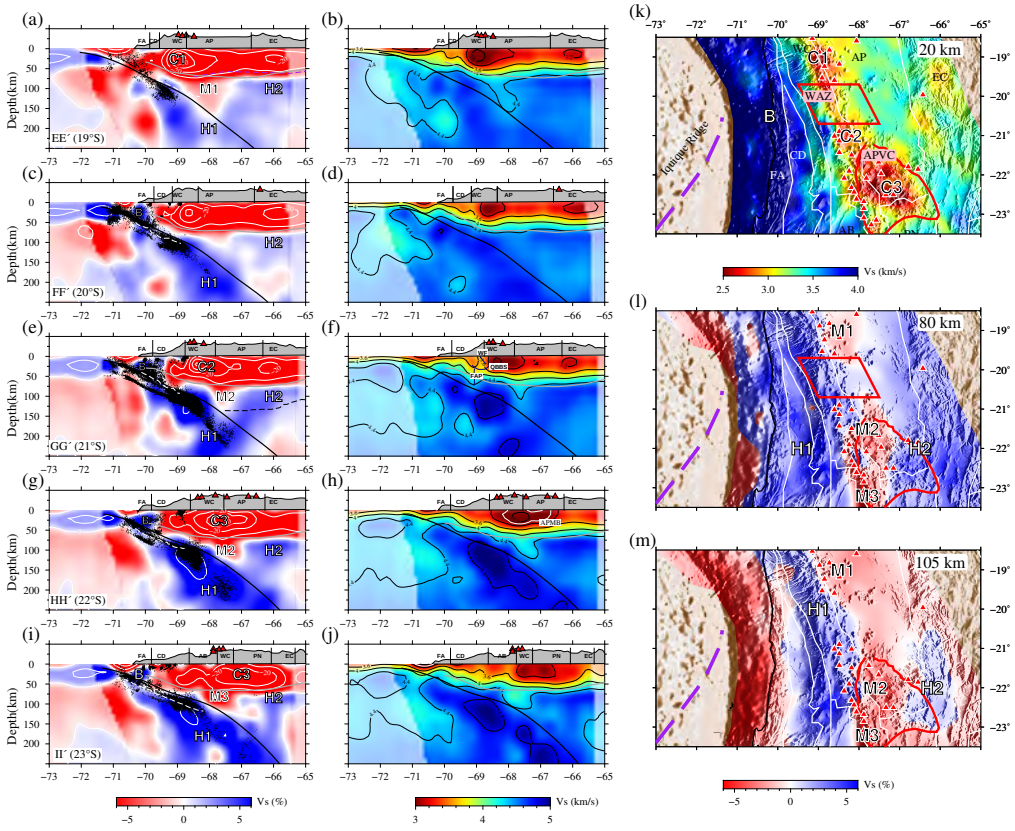

Figure 12. (a), (c), (e), (g) and (i) are cross sections of the V_S perturbations for profiles EE' – II'. (b), (d), (f), (h) and (j) are cross sections of the absolute V_S. Black dots denote the seismicity from Sippl et al. (2018). The Moho is extracted from Tassara and Echaurren (2012), denoted by grey lines. Thin black dashed lines beneath anomaly H2 in (e) is the LAB depth contour extracted from Heit, Sodoudi, et al. (2007). Solid blue lines within the crust beneath the CD mark the positions of West Fissure, QBBS and Fluid Ascent Path (FAP) (Bloch et al., 2014; Yoon et al., 2009) along GG' in (f) and the white dashed lines in (c)-(i) are oceanic Moho retrieved from X. Yuan et al. (2000). Solid black lines denote the slab contour from Slab2.0. (k),(l) and (m) are zoomed-in horizontal slices for the crust and upper mantle. Other elements as in Fig. 11.

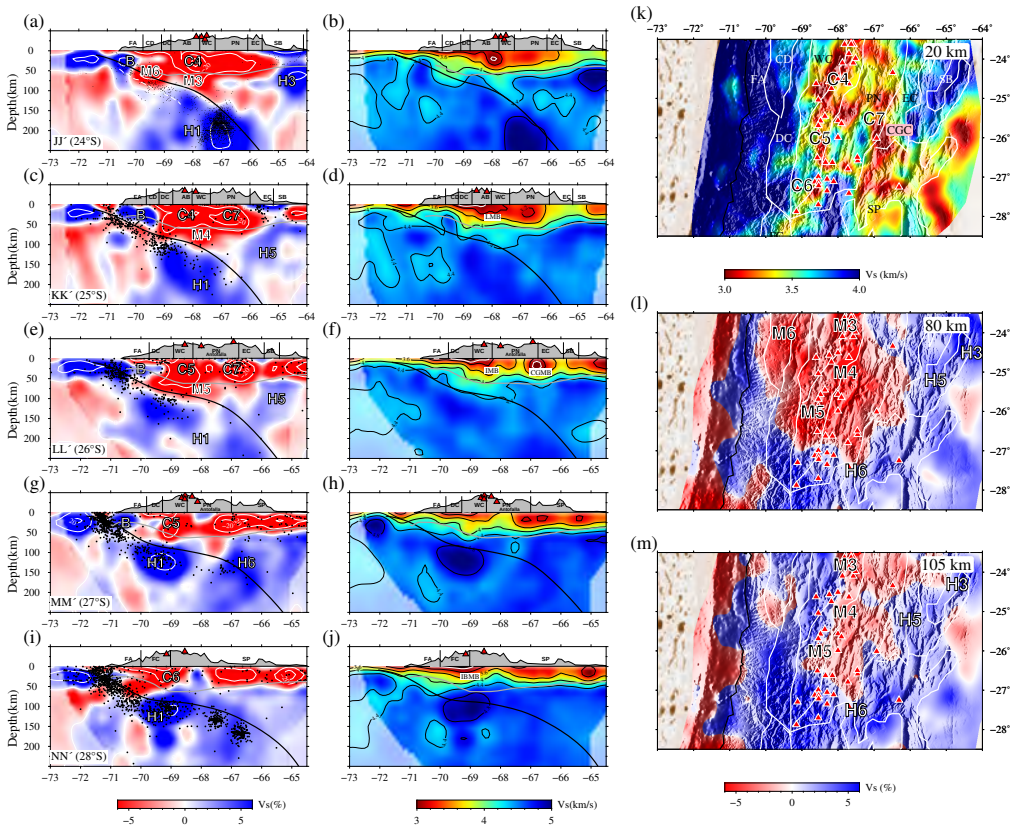

Figure 13. (a), (c), (e), (g) and (i) are cross sections of V_S perturbations for profiles JJ'–NN'. (b), (d), (f), (h) and (j) are cross-sections of the absolute V_S. Black dots denote the seismicity retrieved from ISC-EHB catalogue `http://www.isc.ac.uk/isc-ehb/`. Grey solid lines denote the Moho depth retrieved from Tassara and Echaurren (2012). Solid black lines denote the slab contour from Slab2.0. The white dashed line in (a) is the oceanic Moho retrieved from X. Yuan et al. (2000). (k), (l) and (m) Zoomed-in horizontal slices for the crust and upper mantle. Other elements as in Fig. 11.

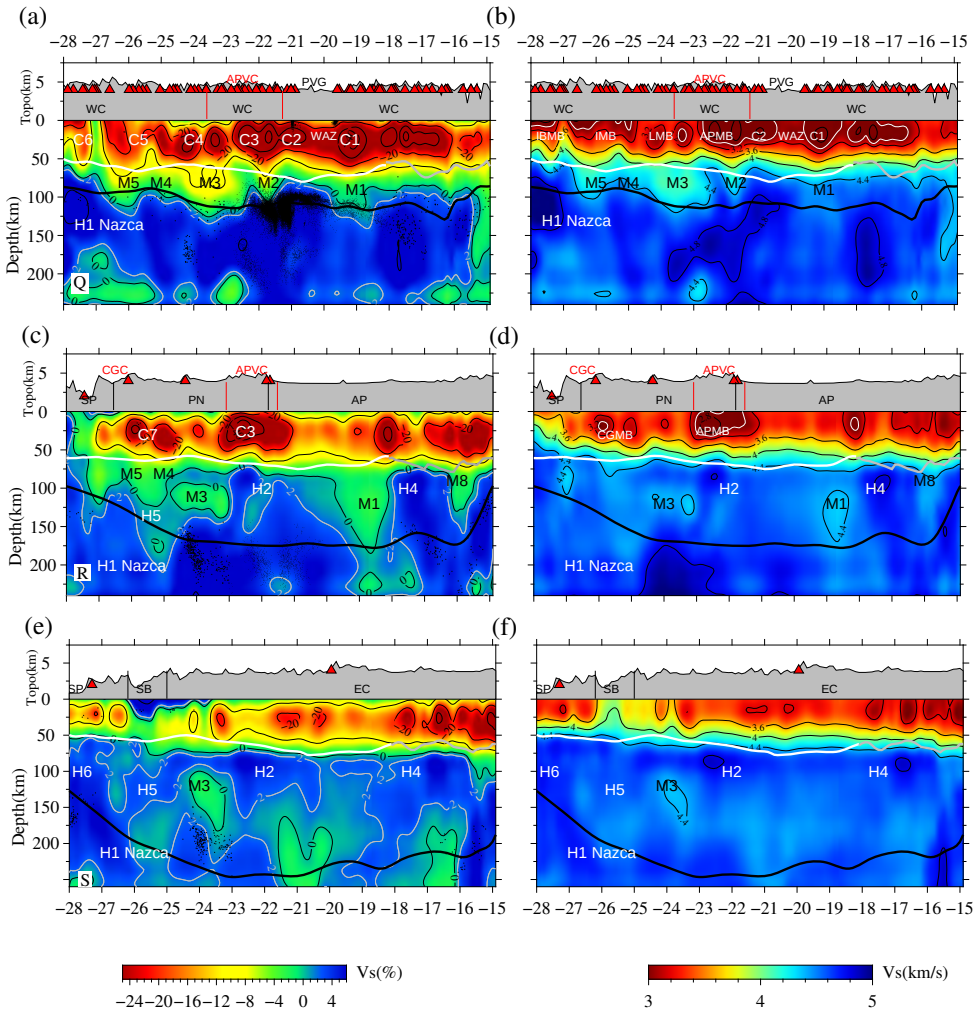

Figure 14. Cross sections along the frontal arc and back-arc area, defined by Q, R and S from the west to the east defined in Figure 9b. (a), (c) and (e) are cross-sections of V_S perturbations. (b),(d) and (f) are absolute velocity models. White solid lines denote the Moho depth derived from Tassara and Echaurren (2012) while grey lines are Moho from Bishop et al. (2017) for southern Peru, north of 18°S. Black lines are Nazca slab contours extracted from Slab2.0. The seismicity denoted by black dots are retrieved from Kumar et al. (2016) north of 18°S, Sippl et al. (2018) for 18°S–23°S and ISC-EHB catalog south of 23°S. The seismicity plotted along each profile has a half-width of 0.8° around the central longitude.

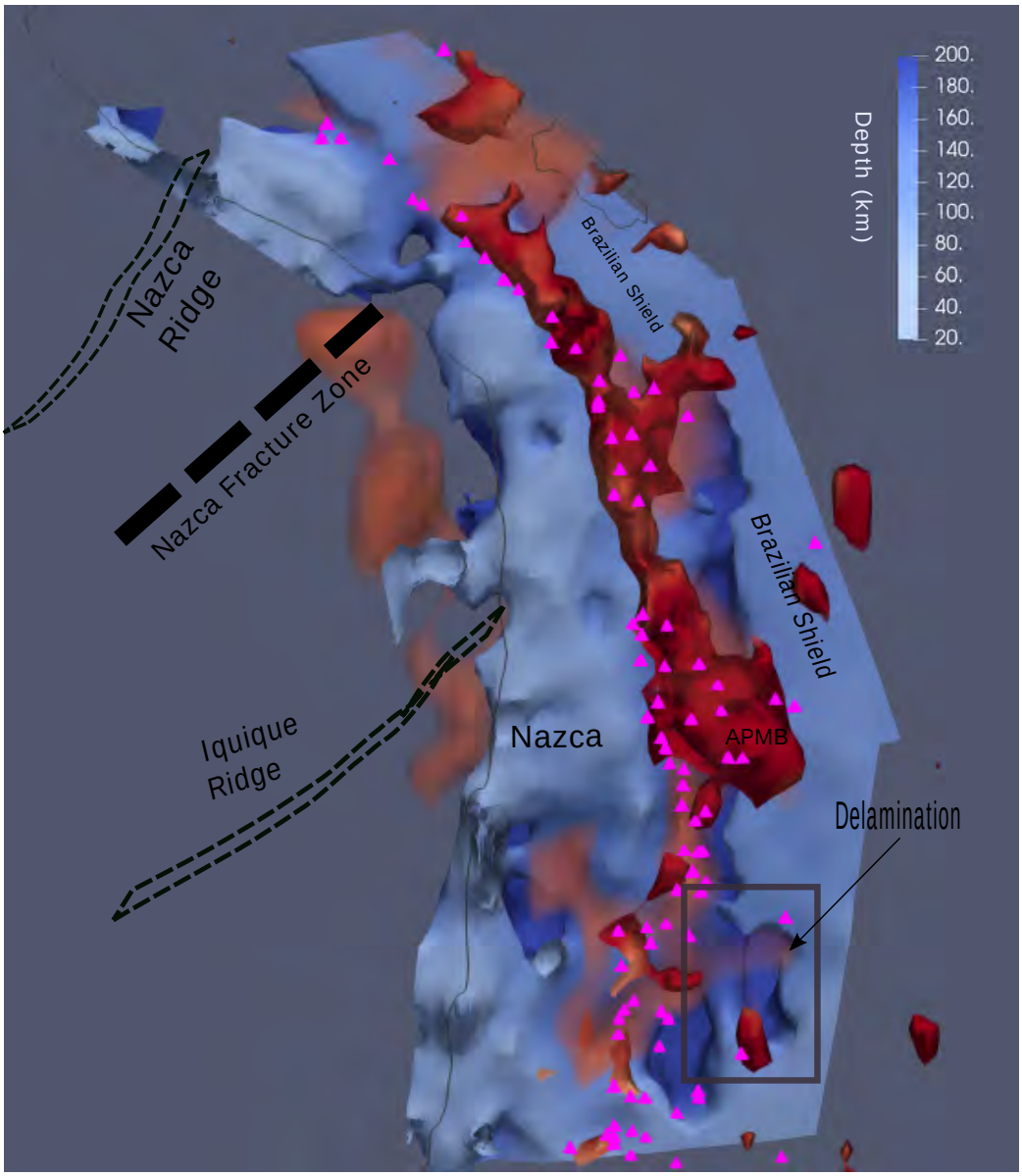

Figure 15. Conceptual model illustrated with volume contours retrieved from isotropic V_S. The regions enclosed by red surfaces represent low velocity anomalies (partial melting) within the crust and orange denotes low velocity anomalies within the uppermost mantle, representing the mantle wedge; blue marks high velocity regions interpreted as Nazca and continental lithosphere, color-scaled by depth. Volcanoes are denoted by magenta triangles.